



Study of Variability in Long-term Multiwavelength Optical Lightcurves of Blazar AO 0235+164

Abhradeep Roy¹ , Alok C. Gupta^{2,3} , Varsha R. Chitnis¹ , Sergio A. Cellone^{4,5} , Claudia M. Raiteri⁶ , Gustavo E. Romero^{5,7} , Paul J. Wiita⁸ , Anshu Chatterjee¹ , Jorge A. Combi^{5,7,9} , Mai Liao^{10,11} , Arkadipta Sarkar¹² , and Massimo Villata⁶

¹ Department of High Energy Physics, Tata Institute of Fundamental Research, Homi Bhabha Road, Mumbai-400005, India; abhradeep.1996@gmail.com, abhradeep.roy@tifr.res.in

² Aryabhata Research Institute of Observational Sciences (ARIES), Manora Peak, Nainital 263001, India

³ Key Laboratory for Research in Galaxies and Cosmology, Shanghai Astronomical Observatory, Chinese Academy of Sciences, Shanghai 200030, People's Republic of China

⁴ Complejo Astronómico El Leoncito (CASLEO, CONICET-UNLP-UNC-UNSJ), San Juan, Argentina

⁵ Facultad de Ciencias Astronómicas y Geofísicas, Universidad Nacional de La Plata, La Plata, Buenos Aires, Argentina

⁶ INAF-Osservatorio Astrofisico di Torino, Via Osservatorio 20, I-10025 Pino Torinese, Italy

⁷ Instituto Argentino de Radioastronomía (CCT-La Plata, CONICET; CICPBA; UNLP), Buenos Aires, Argentina

⁸ Department of Physics, The College of New Jersey, 2000 Pennington Road, Ewing, NJ 08628-0718, USA

⁹ Departamento de Ingeniería Mecánica y Minera, Universidad de Jaén, Campus Las Lagunillas s/n Ed. A3 Jaén, E-23071, Spain

¹⁰ CAS Key Laboratory for Researches in Galaxies and Cosmology, Department of Astronomy, University of Science and Technology of China, Hefei, Anhui 230026, People's Republic of China

¹¹ School of Astronomy and Space Science, University of Science and Technology of China, Hefei, Anhui 230026, People's Republic of China

¹² Deutsches Elektronen-Synchrotron, Platanenallee 6, D-15738 Zeuthen, Germany

Received 2022 October 1; revised 2022 December 12; accepted 2023 January 3; published 2023 February 23

Abstract

We present a long-term and intraday variability study of optical multiwaveband (*UBVRI*) data from the blazar AO 0235+164 collected by various telescopes for ~ 44 yr (1975–2019). The blazar was found to be significantly variable over the years in all wave bands with a variation of about 6 mag between its low and active states. The variations in the different wave bands are highly correlated without any time lag. We did not observe any significant trend in color variation with time, but we observed a bluer-when-brighter trend between the $B - I$ color index and the R magnitude. Optical *BVR*-band spectral energy distributions always show a convex shape. Significant intraday variability was frequently seen in the quasi-simultaneous observations of AO 0235+164 made on 22 nights in the R and V bands by the CASLEO and CAHA telescopes during 1999–2019. We also estimated a central supermassive black hole mass of $7.9 \times 10^7 M_{\odot}$ by analyzing the broad Mg II emission line in AO 0235+164's spectrum. We briefly explore the probable physical scenarios responsible for the observed variability.

Unified Astronomy Thesaurus concepts: Galaxies (573); Active galaxies (17); BL Lacertae objects (158); Quasars (1319)

Supporting material: animation

1. Introduction

Blazars belong to the radio-loud class of active galactic nuclei (AGNs). This extremely variable class is the union of BL Lacertae (BL Lac) objects and flat-spectrum radio quasars (FSRQs). Blazars host a large-scale relativistic jet of plasma pointing very close to the observer's line of sight (Urry & Padovani 1995). The jet is launched from the very near vicinity of a supermassive black hole (SMBH) of mass 10^6 – $10^{10} M_{\odot}$ at the center of the AGN (e.g., Woo & Urry 2002). Blazars are characterized by highly variable emission throughout the whole electromagnetic (EM) spectrum, from radio to γ -rays, and their spectral energy distributions (SEDs) are characterized by two broad humps (Fossati et al. 1998). Blazars display high and variable polarization from radio to optical bands and emit predominately nonthermal emission in the entire EM spectrum. The low-energy hump is ascribed to synchrotron radiation from relativistic leptons, whereas the high-energy hump arises from

inverse Compton processes and sometimes from hadronic processes (e.g., Marscher 1983; Mucke et al. 2003; Romero et al. 2017, and references therein).

Blazars display flux variability on diverse timescales ranging from a few minutes to several years. Blazar variability has often been divided into three categories, depending on the cadence of the observations: (i) microvariability (Miller et al. 1989), or intraday variability (IDV) (Wagner & Witzel 1995), or intranight variability (Sagar et al. 2004), focusing on variability over a day or less; (ii) short-term variability (STV), focusing on variability over days to weeks; and (iii) long-term variability, focusing on timescales of months to years (e.g., Gupta et al. 2004).

The BL Lac object AO 0235+164 is at redshift $z = 0.94$ (Cohen et al. 1987). Optical spectroscopic and photometric observations of the object have discovered two foreground-absorbing systems at $z = 0.524$ and $z = 0.851$ (Cohen et al. 1987; Nilsson et al. 1996; Raiteri et al. 2007). The flux of the source can be both absorbed and contaminated by these foreground systems, and the stars in them may act as gravitational microlenses that could contribute to the observed variability. Abraham et al. (1993) did deep CFHT imaging of

AO 0235+164 and reported that the source is weakly amplified by macrolensing/microlensing by stars in the foreground.

AO 0235+164 has been extensively observed from radio to γ -ray bands either in individual EM bands or quasi-simultaneously in multiple EM bands and has shown variations in all those bands on diverse timescales (e.g., Madejski et al. 1996; Rabbette et al. 1996; Takalo et al. 1998; Qian et al. 2000; Romero et al. 2000; Webb et al. 2000; Raiteri et al. 2006, 2008; Gupta et al. 2008; Hagen-Thorn et al. 2008; Agudo et al. 2011; Ackermann et al. 2012; Fan et al. 2017; Kutkin et al. 2018; Wang & Jiang 2020, and references therein). It is one of the blazars that have displayed very high and variable optical/near-infrared (NIR) polarization up to $\sim 45\%$ (e.g., Impey et al. 1982; Stickel et al. 1993; Fan & Lin 1999; Cellone et al. 2007; Ikejiri et al. 2011; Itoh et al. 2016, and references therein). In the Hamburg quasar monitoring program, this source was observed in the optical R band during 1988–1993, during which a 2.36 ± 0.25 mag variation was detected; a particularly strong brightening in the source of ~ 1.6 mag was reported during 1989 February 20–22 (Schramm et al. 1994). In six nights of optical B - and V -band observations during 1992 September 21–27 the blazar was found in an unusually bright state and IDV was detected in both the B and V bands (Rabbette et al. 1996). On another occasion, six nights of quasi-simultaneous V - and R -band observations in 1999 November revealed IDV with an amplitude of $\sim 100\%$ over timescales of a day, while 0.5 mag changes were reported in both bands on a single night (Romero et al. 2000). In multicolor optical/NIR photometric ($BVRJHK$) and R -band optical polarimetric observations of AO 0235+164 during its 2006 December outburst, variability on IDV timescales was detected, with an increasing minimum timescale of variability from optical to NIR wavelengths; such variations were even detected in the optical polarization (Hagen-Thorn et al. 2008). In three nights of optical observations of the blazar in 2007 January–March, IDV and STV were detected (Gupta et al. 2008).

In quasi-simultaneous optical (V - and R -band) and radio (22 GHz) observations of AO 0235+164 during 1993–1996, the variability in the optical bands showed amplitudes up to 1.5 mag on STV timescales; although the radio variability was less dramatic, in general, it followed the optical behavior (Takalo et al. 1998). For the 1997 AO 0235+164 outburst, quasi-simultaneous multiwavelength (MW) (radio, optical, NIR, and X-ray) observations were carried out. It was found that the source varied nearly simultaneously over 6 decades in frequency during the outburst and this result was explained in terms of a microlensing event (Webb et al. 2000).

An analysis of this source’s variability over ~ 25 yr led to the suggestion of a ~ 5.7 yr quasiperiodicity of the main radio and optical flares (Raiteri et al. 2001); however, the putative next outburst, predicted to peak around 2004 February–March, did not occur, and a new analysis of the optical lightcurves on a longer time span revealed a characteristic variability timescale of ~ 8 yr, which was also present in the radio data (Raiteri et al. 2006). Recently, optical R -band photometric data taken during 1982–2019 showed five cycles of double-peaked periodicity of ~ 8.13 yr with the secondary peak following the primary one within $\sim (1.5\text{--}2.0)$ yr (Roy et al. 2022). In another MW campaign from radio to UV bands in 2006–2007, a huge NIR–optical–UV outburst with a brightness increase of ~ 5 mag during 2007 February 19–21 was detected (Raiteri et al. 2008). During a major outburst seen in 2009, changes in the radio,

optical, X-ray, and γ -ray bands were found to be strongly associated (Agudo et al. 2011). In another simultaneous MW observing campaign of this blazar between 2008 September and 2009 February, γ -ray activity was found to be well correlated with a series of NIR/optical flares, accompanied by an increase in the optical degree of polarization; the X-ray lightcurve showed a different 20 day high state of an unusually soft spectrum that did not match the extrapolation of the optical/UV synchrotron spectrum (Ackermann et al. 2012).

AO 0235+164 is one of the sources that used to be called optically violently variable. There are several such objects, like 3C 279, 3C 454.3, 4C 29.45, CTA 102, and other BL Lacertae objects. Long-term achromaticity and zero lags have widely been found for these sources (Fan et al. 2006; Bonning et al. 2012; Guo et al. 2015; Raiteri et al. 2017; Zhang et al. 2021). AO 0235+164 is peculiar because it is commonly considered a BL Lac object, one of the farthest known, but it shares properties with FSRQs. It is also a complex source because its light is contaminated by the southern AGN, ELISA, and absorbed by an intervening galaxy. This paper undertakes a detailed analysis of the source’s optical brightness and spectral variability over a very long time span (~ 5 decades) as well as an investigation of its central engine. Our aim is to shed light on the long- and short-term behavior of an emblematic BL Lac object through a detailed analysis of what is likely the most massive data set ever assembled for an object of this kind. The paper is organized as follows. In Section 2, we provide descriptions of the observations of AO 0235+164. Section 3 gives our data analysis methods and results. We present a discussion and conclusions in Sections 4 and 5, respectively.

2. Observations

Most of the optical $UBVRI$ observations of AO 0235+164 we employ in this work are taken from the Whole Earth Blazar Telescope¹³ (WEBT; Villata et al. 2002; Raiteri et al. 2017), which is an international collaboration of optical, NIR, and radio observers. WEBT has organized several monitoring campaigns on the blazar AO 0235+164, with the participation of tens of observers and telescopes all around the world. This source has been studied by WEBT and by its GLAST–AGILE Support Program (GASP) (Villata et al. 2008, 2009), which was started in 2007 to record quasi-simultaneous data of various blazars observed by the AGILE and Fermi (formerly GLAST) satellites. WEBT/GASP data on AO 0235+164 have been published in Raiteri et al. (2001, 2005, 2006, 2008) and in Ackermann et al. (2012). Raiteri et al. (2005) have prescribed ways to remove the contribution of the southern galaxy ELISA from the observed optical flux densities and estimated the amount of absorption toward the source in excess of that from our Galaxy in the X-ray, ultraviolet, optical, and NIR bands.

The WEBT and GASP data were calibrated following a common prescription, i.e., with the same photometry for the same reference stars. For the calibration of the AO 0235+164 observations, the adopted photometric sequence included stars 1, 2, and 3 from Smith et al. (1985). To build a reliable lightcurve for further analysis, clear outliers were removed and minor systematic offsets between various data sets were corrected.

AO 0235+164 was also observed with the 2.2 m telescope of Calar Alto Astronomical Observatory (CAHA, Spain) in 2005 November–December, using the CAFOS instrument in

¹³ <https://www.oato.inaf.it/blazars/webt>

imaging polarimetry mode, and photometric data were obtained by adding up the ordinary and extraordinary fluxes from each individual image (Cellone et al. 2007). Photometric data were also obtained with the 2.15 m telescope at Complejo Astronómico El Leoncito (CASLEO, Argentina) along several runs in 1999 November, 2000 December, 2004 August, and 2005 January. Results from these data were published in Romero et al. (1999, 2000, 2002) and in two papers by the WEBT collaboration focused on this blazar (Raiteri et al. 2005, 2006). Data from a more recent (2019 December) observing run with the same telescope were used in Roy et al. (2022). Magnitude calibration to the standard system was done using our own photometry of Landolt’s (2009) fields as well as standard stars in the field of AO 0235+164 (Smith et al. 1985; Gonzalez-Perez et al. 2001).

We also collected the publicly available optical R - and V -band data of AO 0235+164, taken at Steward Observatory,¹⁴ University of Arizona. These measurements employed the 2.3 m Bok and 1.54 m Kuiper telescopes between 2008 October 4 and 2018 February 12, using the SPOL CCD Imaging/Spectropolarimeter attached to those two telescopes. Details about the instrument, observation, and data analysis are given in Smith et al. (2009). In addition, we included the optical BVR data from the Small and Moderate Aperture Research Telescope System (SMARTS) public archive.¹⁵ The SMARTS consortium is part of the Cerro Tololo Inter-American Observatory (CTIO), Chile, and has been observing Fermi Large Area Telescope-monitored blazars in the optical B , V , and R and NIR J and K bands. Details about the SMARTS instruments, observations, and data analysis procedures are given in Bonning et al. (2012). These standard magnitudes observed by CASLEO, CAHA, SMARTS, and the Steward Observatory were further corrected for the southern galaxy ELISA following Raiteri et al. (2005). We also added other R -band optical photometric data from the literature (Takalo et al. 1998; Hagen-Thorn et al. 2008).

3. Data Analysis Methods and Results

We combined all the optical U -, B -, V -, R -, and I -band data to plot the long-term (1974–2020) MW lightcurves of blazar AO 0235+164 (Figure 1). We removed observations with errors of more than 0.1 mag and studied long-term variability and IDV, color variation, spectral properties, and interband correlations.

3.1. Flux Variability Studies

We used different tools on the observed optical magnitudes to quantify the variability timescales and the corresponding significance in multiple optical wave bands.

3.1.1. The χ^2 -test

For a time series of flux density observations, χ^2 is defined as

$$\chi^2 = \sum_{i=1}^N \frac{(\mathcal{M}_i - \bar{\mathcal{M}})^2}{\varepsilon_i^2} \quad (1)$$

where \mathcal{M}_i is the magnitude obtained at the i th observation, ε_i is the corresponding error in measurement, and $\bar{\mathcal{M}}$ is the average magnitude. If the obtained χ^2 value is higher than the critical χ^2 value at the 99.9% significance level, we consider the source to be variable. The critical value ($\chi_{0.999,d}^2$) depends on the degrees of freedom (d) of the data set. The reduced χ^2 values listed in Table 1 indicate that the source exhibits significant flux variations in all the optical wave bands.

3.1.2. Variability Amplitude

According to the relation given by Heidt & Wagner (1996), we estimated the variability amplitudes (V_M) in percentage for the lightcurves in different wavelengths using the following formula:

$$V_M = 100 \times \sqrt{(\mathcal{M}_{\max} - \mathcal{M}_{\min})^2 - 2\bar{\varepsilon}^2} \quad (\%) \quad (2)$$

where \mathcal{M}_{\max} and \mathcal{M}_{\min} are the maximum and minimum observed magnitudes in a lightcurve, respectively, while $\bar{\varepsilon}$ is the average error in magnitude measurements. We list the calculated variability of amplitudes in Table 1.

3.1.3. Correlation Study

To study the interband correlations, we first generated 15 minute binned optical $UBVRI$ lightcurves, and plotted the average U , B , V , and I magnitudes against the average R magnitudes for the time bins when the source was observed at both wave bands (Figure 2). The magnitude versus magnitude plots show very good linear correlations. To take the uncertainty of magnitude measurements into account, we simulated 10,000 data sets assuming that each magnitude measurement was Gaussian distributed. Then we calculated the mean and standard deviation of the Pearson correlation coefficients of all simulated data sets. We obtained high correlations (>0.9) with small uncertainties (<0.003) between all wave bands.

Moreover, to find any time lag between the correlated optical lightcurves we computed the discrete correlation function (DCF) from the unbinned MW lightcurves, as the lightcurves consist of discrete data points. Following the method of Edelson & Krolik (1988), we computed the unbinned DCF (UDCF) between the i th data point in one wave band (a) and the j th data point in another (b) as

$$\text{UDCF}_{ij} = \frac{(a_i - \bar{a})(b_j - \bar{b})}{\sigma_a \sigma_b}, \quad (3)$$

where \bar{a} and \bar{b} are the mean of the observed magnitudes, and σ_a and σ_b are the standard deviations of the corresponding data sets. Next, we calculated the DCF at a certain time lag τ by averaging the UDCF_{ij} whose corresponding time lags $\Delta t_{ij} = t_i^a - t_j^b$ lie within the range $[\tau - \frac{\Delta\tau}{2}, \tau + \frac{\Delta\tau}{2}]$ ($\Delta\tau$ is the time lag bin width), such that

$$\text{DCF}(\tau) = \frac{1}{n} \sum \text{UDCF}_{ij}(\tau). \quad (4)$$

Following the suggestion of White & Peterson (1994), we computed the mean magnitudes (\bar{a} and \bar{b}) and the standard deviations (σ_a and σ_b) in Equation (3) using only those data points that fall within a given time lag bin, as the mean and standard deviation keep on changing for a time series that originates from a stochastic process such as blazar emission.

¹⁴ <http://james.as.arizona.edu/~smith/Fermi/DATA/Rphotdata.html>

¹⁵ <http://www.astro.yale.edu/smarts/glast/home.php#>

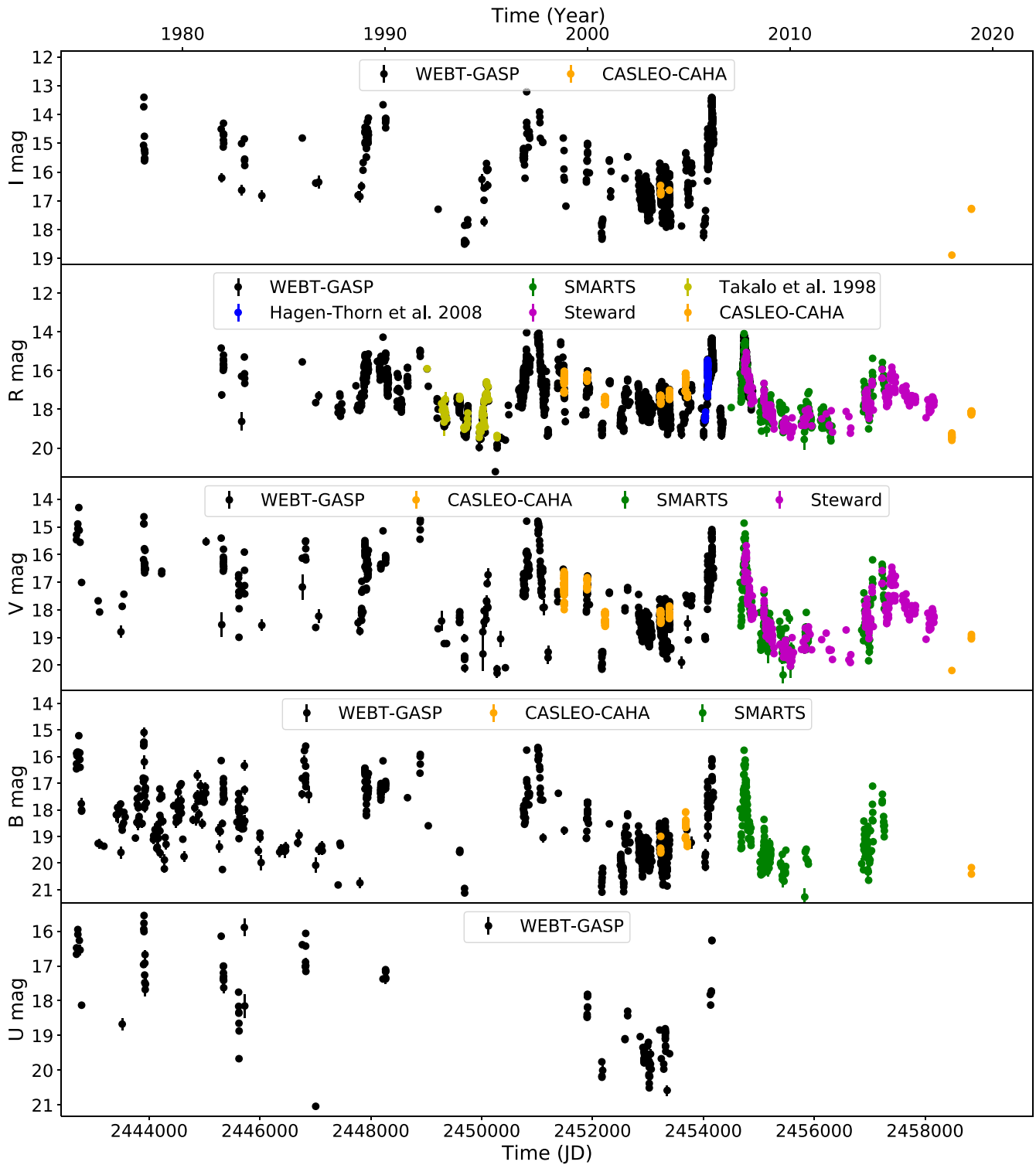


Figure 1. Long-term MW optical (*U*, *B*, *V*, *R*, and *I*) lightcurves of AO 0235+164 observed from multiple ground-based telescopes between JD 2,442,689 (1975 October 3) and JD 2,458,835 (2019 December 17).

The error in the $DCF(\tau)$ computation in each bin was calculated as

$$\sigma_{DCF}(\tau) = \frac{1}{M-1} \sqrt{\sum_{k=1}^M (UDCF_k - DCF(\tau))^2}. \quad (5)$$

Figure 3 shows the DCFs of the *UBVI* bands with respect to the *R*-band observations. In all cases, the DCFs peak at zero time lag, except the *U*-band versus *R*-band DCF due to poor data sampling in the *U* band. This explains the strong linearity in Figure 2 and implies that the emission at all optical wave bands

Table 1
Results of Flux Variability on Optical *UBVRI* Long-term Lightcurves of
AO 0235+164

Optical Filter	Total Obs.	$\chi^2_{\text{red.}}$	$\chi^2_{0.999,\text{red.}}$	Status	Variability Amplitude (%)
<i>U</i>	109	904.5	1.47	V	548.8
<i>B</i>	894	3246.7	1.15	V	590.9
<i>V</i>	1403	5968.4	1.12	V	589.0
<i>R</i>	5675	8715.5	1.06	V	718.8
<i>I</i>	1173	3555.2	1.13	V	567.5

Note. In the fifth column “V” represents a variable status.

comes from the same region in the jet and is produced by the same radiation mechanism.

3.1.4. Color Variations

The term “color” denotes the magnitude difference between two quasi-simultaneous observations at two different wave bands. We plot the variation of the optical colors ($U - B$, $B - V$, $V - R$, $R - I$, and $B - I$) with time and the R magnitude in Figure 4. We list the results of a straight-line ($Y = mX + c$) fitting to all these plots in Tables 2 and 3. The linear fits of the color versus time plots do not show any trend, except for the rather sparsely sampled ($B - I$) color, which has a high slope (4.16×10^{-5}) in Figure 4(a), along with the highest Pearson correlation coefficient (0.45), and the lowest null hypothesis probability (3.41×10^{-11}). Among the color versus magnitude relations, the strongest relationship is between ($B - I$) and R (Figure 4(b)), having a positive slope (6.23×10^{-2}) with the highest Pearson coefficient (0.37) and the lowest p -value (1.69×10^{-7}) (Table 3), which indicates a bluer-when-brighter trend when the widest range of available colors is considered.

3.1.5. Spectral Variations and SEDs

We plotted the optical *BVR* SEDs for the nights when observations were taken at all of these three filters. Following the prescription of Raiteri et al. (2005), we took into account the total absorption by the Milky Way and the foreground absorber at $z = 0.524$, and subtracted the extinction magnitudes ($A_U = 2.519$, $A_B = 1.904$, $A_V = 1.473$, $A_R = 1.260$, and $A_I = 0.902$) from the calibrated magnitudes of the respective wave bands and then converted them into extinction-corrected flux densities, F_ν . The accompanying video contains the 1 day average optical SEDs for those 360 nights (an example frame is shown in Figure 5). Figure 6 shows a few examples of SEDs of low-, moderate-, and high-flux states, plotted in $(\nu F_\nu - \nu)$ format. Mostly, the SEDs have a declining shape following a power law. However, there are evidences of spectral hardening on several nights (e.g., JD 2,445,337, JD 2,445,721, JD 2,448,889, JD 2,452,901, and JD 2,453,230).

From the 1 day binned MW lightcurves we calculated the spectral indices (α_{VR}) for all the days when the source was observed in both the V and R bands, using the formula given by Wierzcholska et al. (2015) on extinction-corrected magnitudes, as

$$\alpha_{VR} = \frac{0.4(V - R)}{\log(\nu_V / \nu_R)}, \quad (6)$$

where ν_V and ν_R , respectively, represent the effective frequencies of the V - and R -band filters (Bessell 2005). We plot the variation

of the spectral indices with time and the R -band magnitude in Figure 7 and list the results of linear fits, Pearson coefficients, and null hypothesis probabilities in Table 4. We do not find any significant long-term variation of the spectral index with time, nor is there a correlation with the R magnitude.

3.2. IDV

We applied four frequently used statistical tests for IDV-scaled C -criterion, scaled F -test, power-enhanced F -test, and nested analysis of variance (ANOVA) test (de Diego 2014; de Diego et al. 2015; Zibecchi et al. 2017, 2020)—to detect statistically significant intraday flux variability in AO 0235+164 lightcurves observed by the CASLEO and CAHA telescopes. These tests mainly compare variations in blazar magnitudes with variations in the magnitudes of one or more stars within the field of view of the blazar and have different advantages and disadvantages. We collected data from multiple field stars along with the blazar data (Table 5). We applied the first three methods on the intraday differential lightcurves (DLCs) of AO 0235+164, where at least 10 observations were recorded per night with at least one optical filter between 1999 November 2 and 2019 December 17. We employed the nested ANOVA test only on lightcurves having at least 20 observations per night.

3.2.1. Scaled C -criterion

Differential photometry, where blazar magnitudes are compared to those of one or more stars in the same field of view, is the usual technique for obtaining blazar lightcurves free from the effects of any nonastrophysical fluctuations. The simplest differential photometry involves a single comparison star, while a second star, whose magnitudes are measured against the same comparison star, is used for a stability check. We denote as B, S1, and S2 the blazar, comparison star, and control star, respectively. The variability test requires two DLCs: (blazar–comparison star) and (control star–comparison star). The latter is believed to be affected only by instrumental fluctuations as any known or suspected variable star can be discarded.

Jang & Miller (1997) and Romero et al. (1999) introduced a parameter C defined as $C = \sigma_{B-S1} / \sigma_{S2-S1}$, where σ_{B-S1} and σ_{S2-S1} are the standard deviations in the blazar DLC and control star DLC, respectively. The blazar is considered to be variable with a 99.5% confidence level if C is greater than the critical value of 2.576.

Howell et al. (1988) pointed out that it is important to select nonvariable stars with magnitudes close to the blazar magnitude as comparison and control stars. Otherwise, even if the blazar is nonvariable, there will be a difference between σ_{B-S1} and σ_{S2-S1} due to differences in photon statistics and other random-noise terms (sky and readout noise). To use field stars with different magnitude levels, Howell et al. (1988) suggested calculating a correction factor Γ to scale σ_{S2-S1} to the instrumental level of σ_{B-S1} for proper comparison. Γ can be estimated using the following formula:

$$\Gamma^2 = \left(\frac{N_{S2}}{N_B} \right)^2 \left[\frac{N_{S1}^2(N_B + P) + N_B^2(N_{S1} + P)}{N_{S2}^2(N_{S1} + P) + N_{S1}^2(N_{S2} + P)} \right] \quad (7)$$

where N is the total (sky-subtracted) count within the aperture, while the subindices B, S1, and S2 correspond to the N of the

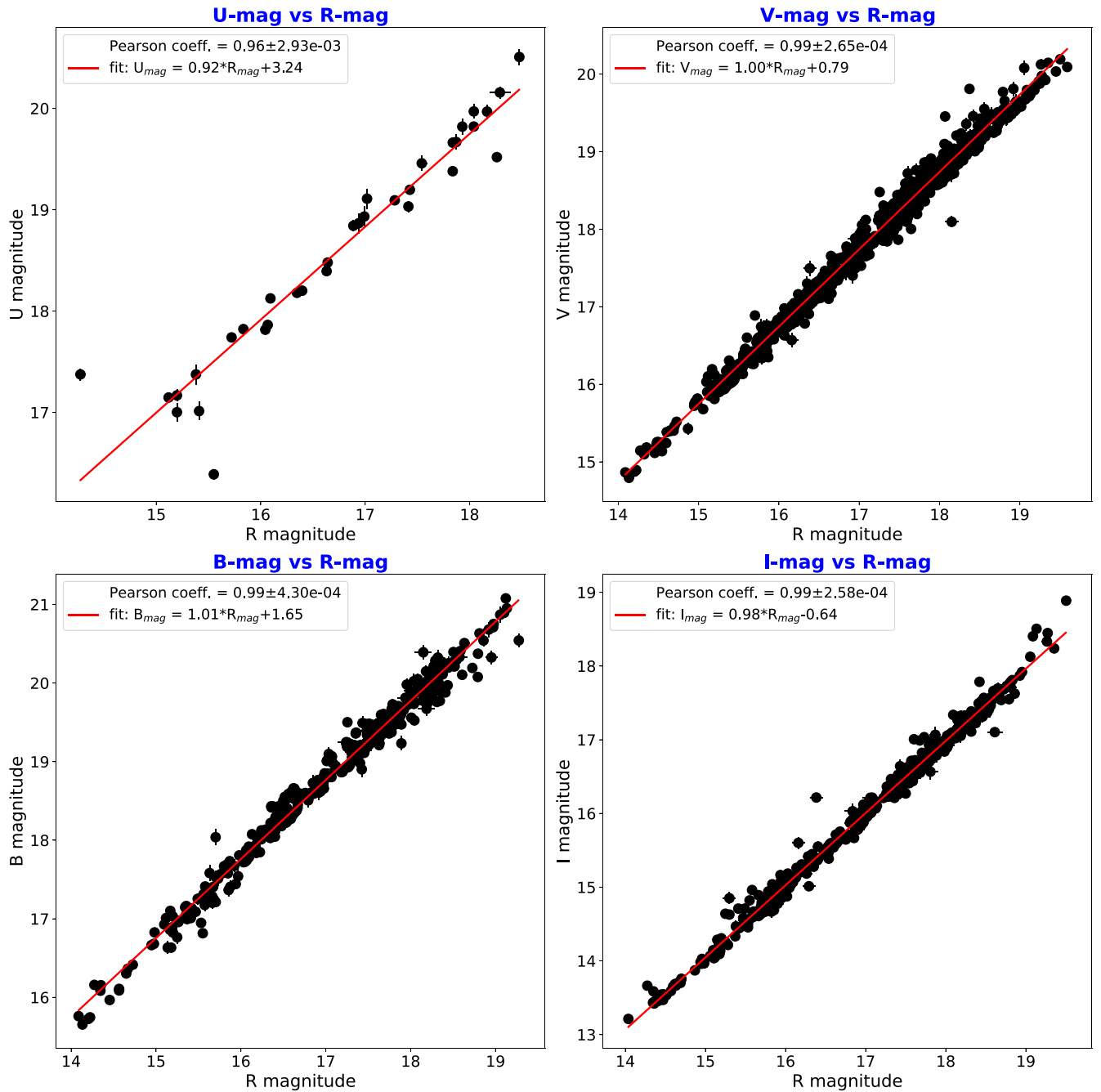


Figure 2. Fifteen-minute-average *UBVI* magnitude vs. *R* magnitude plots for correlation study. *U*-, *B*-, *V*-, and *I*-band observations show a high linear correlation with *R*-band data. All the plots are fitted with straight lines.

blazar, comparison star, and control star, respectively. The factor P contains the common noise terms, $P = n_{\text{pix}}(N_{\text{sky}} + N_{\text{RON}}^2)$, where n_{pix} is the number of pixels within the aperture, N_{sky} is the sky level, and N_{RON} is the readout noise. We used the median values of the N of the objects and sky for calculating Γ . Thus, the scaled C parameter (C_Γ) is defined as

$$C_\Gamma = \frac{C}{\Gamma} = \frac{1}{\Gamma} \left(\frac{\sigma_{\text{B-S1}}}{\sigma_{\text{S2-S1}}} \right). \quad (8)$$

The source is considered variable if $C_\Gamma \geq 2.576$. Even though the C parameter is not a proper statistic, it remains a useful

indicator of stability (de Diego 2014; de Diego et al. 2015; Zibecchi et al. 2017, 2020).

3.2.2. Scaled F -test

The standard F -statistic parameter is $F = \sigma_{\text{B-S1}}^2 / \sigma_{\text{S2-S1}}^2$, where $\sigma_{\text{B-S1}}^2$ and $\sigma_{\text{S2-S1}}^2$ are the variances in the blazar DLC and control star DLC, respectively. The scaled F -statistic F_Γ is given as

$$F_\Gamma = \frac{F}{\Gamma^2} = \frac{1}{\Gamma^2} \left(\frac{\sigma_{\text{B-S1}}^2}{\sigma_{\text{S2-S1}}^2} \right).$$

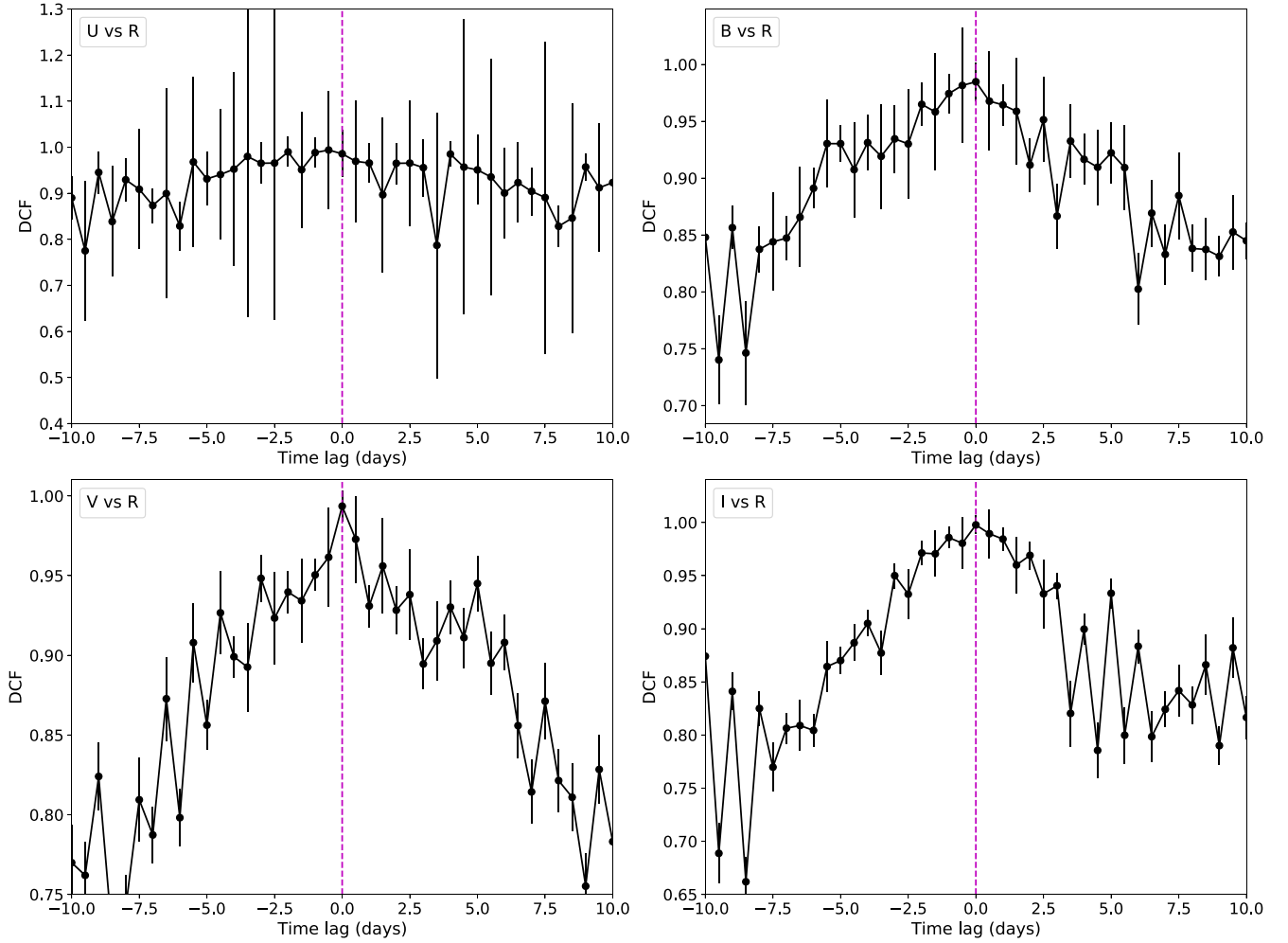


Figure 3. Results of discrete cross-correlation analysis of U , B , V , and I bands with respect to the R band in the full time range.

The F -statistic assumes that the uncertainties in the observations are normally distributed. If $n_{(B-S1)}$ and $n_{(S2-S1)}$ are the sizes of the blazar and control star DLCs, respectively, the degrees of freedom in the numerator and denominator of the F -statistic are $\nu_1 = n_{(B-S1)} - 1$ and $\nu_2 = n_{(S2-S1)} - 1$, respectively. We calculated F_Γ and considered the blazar to be variable with 99.5% confidence if F_Γ was greater than the critical value $F_c^\alpha(\nu_1, \nu_2)$ at $\alpha = 0.005$ (Zibecchi et al. 2017, 2020).

3.2.3. Power-enhanced F -test

The power-enhanced F -test has been used in various recent blazar IDV studies (Pandey et al. 2019, 2020, and references therein). The power-enhanced F -statistic has the advantage of comparing the blazar variance to the combined variance of multiple field stars and is given as (de Diego 2014)

$$F_{\text{enh}} = \frac{s_{\text{blz}}^2}{s_c^2}, \quad (9)$$

where s_{blz}^2 is the variance of the DLC of the blazar with respect to a reference star, and s_c^2 is the combined variance of the comparison stars' DLCs with respect to the reference star.

Thus, s_c^2 is given as

$$s_c^2 = \frac{1}{\left(\sum_{j=1}^k n_j\right) - k} \sum_{j=1}^k \sum_{i=1}^{n_j} s_{j,i}^2. \quad (10)$$

Here, k is the total number of available comparison stars in the DLC, n_j is the number of observations of the j th comparison star, and $s_{j,i}^2$ is the scaled square deviation of the i th observation of the j th comparison star given as

$$s_{j,i}^2 = \Gamma_j (m_{j,i} - \bar{m}_j)^2. \quad (11)$$

Here Γ_j is the scale factor of the j th comparison star DLC computed following Equation (7).

Using the data of the field stars, we first checked the star–star DLCs to identify any spikes due to instrumental errors or improper removal of cosmic rays, and removed them iteratively if they were more than 3 standard deviations from the mean magnitude. We considered a “well-behaved” star with low fluctuations and an average magnitude close to the blazar magnitude as the reference star. The degrees of freedom in the numerator and denominator of the F -statistic are $\nu_1 = n_{\text{blz}} - 1$ and $\nu_2 = \left(\sum_{j=1}^k n_j\right) - k$, respectively. We calculated F_{enh} , and considered the blazar to be variable with 99.5% confidence if F_{enh} was greater than the critical value $F_c(\nu_1, \nu_2)$ at $\alpha = 0.005$.

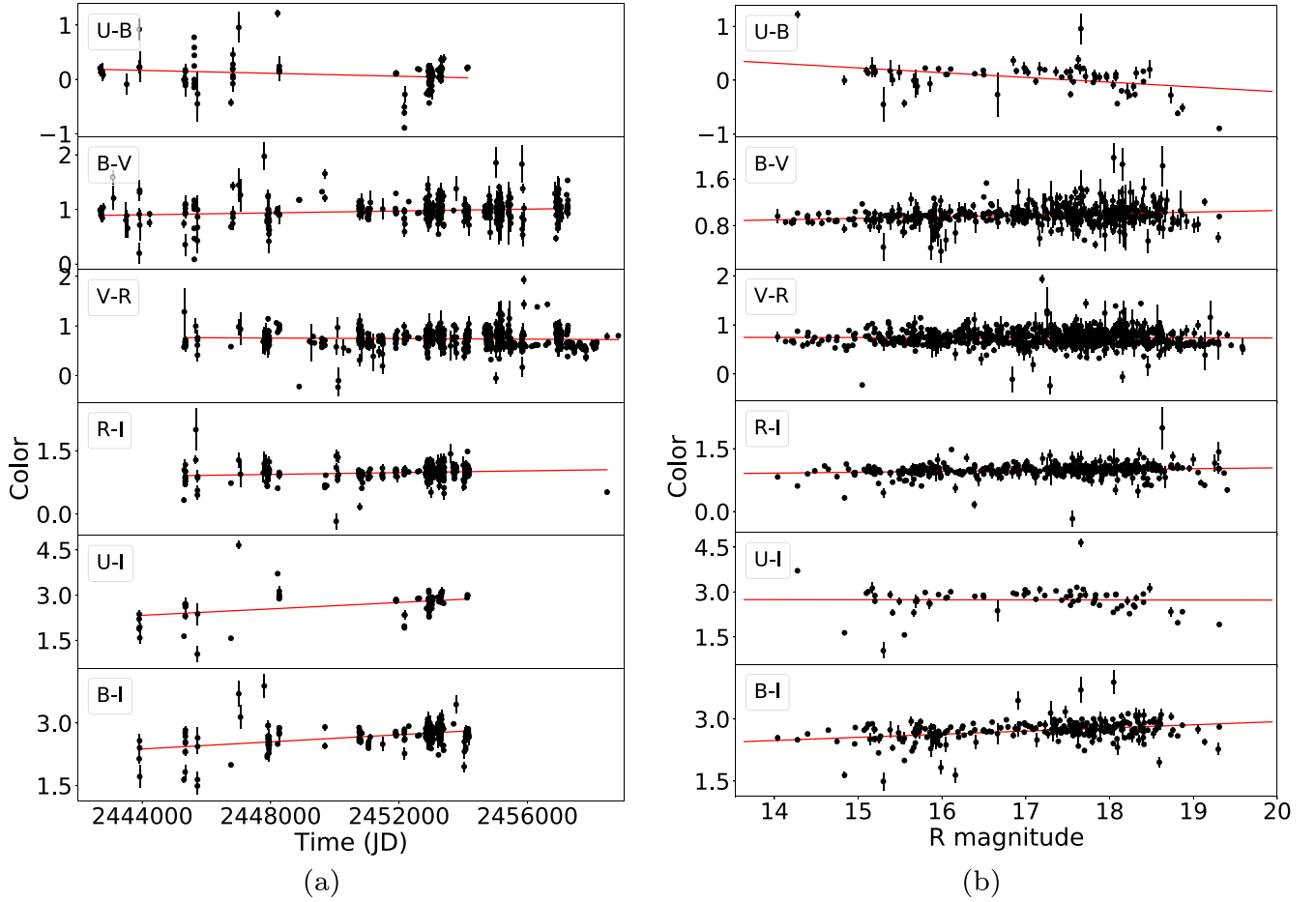


Figure 4. (a) Color variation with time. (b) Color variation with optical R magnitude. The red line in each panel represents the straight-line fit. The fit parameters are given in Tables 2 and 3.

Table 2

Color Variation with Time in Optical $UBVRI$ Long-term Lightcurves of AO 0235+164

CI	m	c	ρ	p
$U - B$	$-1.52\text{E-}05$	$3.74\text{E+}01$	$-2.06\text{E-}01$	$8.28\text{E-}02$
$B - V$	$6.58\text{E-}06$	$-1.52\text{E+}01$	$1.42\text{E-}01$	$4.79\text{E-}03$
$V - R$	$-5.34\text{E-}06$	$1.38\text{E+}01$	$-9.19\text{E-}02$	$1.39\text{E-}02$
$R - I$	$1.83\text{E-}05$	$-4.40\text{E+}01$	$2.85\text{E-}01$	$1.74\text{E-}08$
$U - I$	$5.63\text{E-}05$	$-1.35\text{E+}02$	$4.03\text{E-}01$	$1.88\text{E-}03$
$B - I$	$4.16\text{E-}05$	$-9.92\text{E+}01$	$4.50\text{E-}01$	$3.41\text{E-}11$

Note. Column headings: CI: color indices; m = slope; c = intercept; ρ = Pearson coefficient; and p = null hypothesis probability for Figure 4(a).

Table 3

Color Variation with R -band Magnitude in Optical $UBVRI$ Long-term Lightcurves of AO 0235+164

CI	m	c	ρ	p
$U - B$	$-1.36\text{E-}01$	$2.37\text{E+}00$	$-5.37\text{E-}01$	$3.35\text{E-}05$
$B - V$	$1.62\text{E-}02$	$7.04\text{E-}01$	$1.41\text{E-}01$	$7.41\text{E-}03$
$V - R$	$-3.54\text{E-}03$	$7.98\text{E-}01$	$-2.58\text{E-}02$	$4.92\text{E-}01$
$R - I$	$1.62\text{E-}02$	$7.00\text{E-}01$	$1.37\text{E-}01$	$7.59\text{E-}03$
$U - I$	$-6.47\text{E-}02$	$3.85\text{E+}00$	$-2.07\text{E-}01$	$1.30\text{E-}01$
$B - I$	$6.23\text{E-}02$	$1.66\text{E+}00$	$3.66\text{E-}01$	$1.69\text{E-}07$

Note. Column headings: CI: color indices; m = slope; c = intercept; ρ = Pearson coefficient; and p = null hypothesis probability for Figure 4(b).

3.2.4. Nested ANOVA Test

In the nested ANOVA test, DLCs of the blazar are generated with respect to all the comparison stars used as reference stars. The details of this method are given in de Diego et al. (2015). The nested ANOVA test needs a large number of points in the lightcurves, strongly limiting its application to densely populated DLCs. We divided the DLCs with at least 20 observations into groups such that each group contains four observations. Equation (4) of de Diego et al. (2015) considers an ideal set of lightcurves where the total number of observations is divisible by the group size. In most of the DLCs in this work, the total number of observations is not an integral multiple of the group size of 4. So, in those cases, the last group contains less than four observations, and we calculated the degrees of freedom accordingly to compute the mean square due to groups (MS_G) and the mean square due to the nested observations in groups ($MS_{O(G)}$). The ANOVA F -statistic is given as $F = MS_G / MS_{O(G)}$. For a significance level of $\alpha = 0.005$, if the F -statistic is greater than the critical value (F_c), the blazar is taken as variable, otherwise as nonvariable, with 99.5% confidence.

We have listed the results of the scaled C -criterion and scaled F -test in Table 6 and those of the power-enhanced F -test and the nested ANOVA test in Table 7. In the case of the scaled C -criterion and F -test, we fixed one particular star as the comparison star for each data set. The source is declared variable with respect to one comparison–control star pair if both

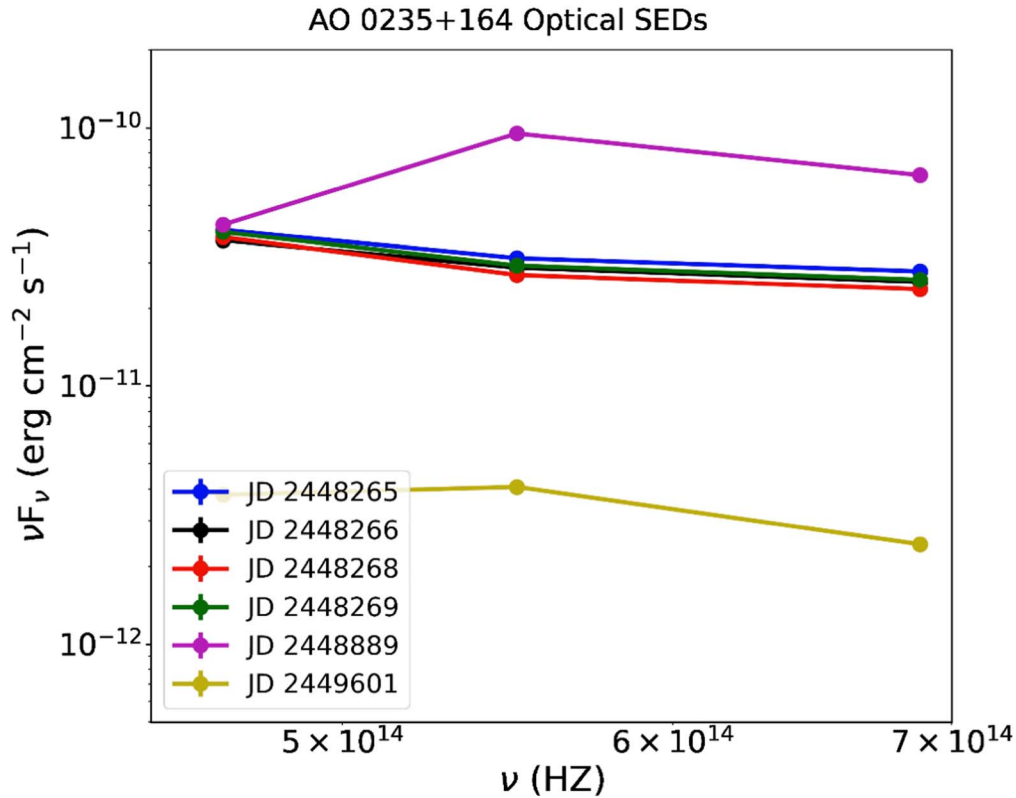


Figure 5. SEDs in an example frame of the AO 0235+164 optical SED animation that is available in the online version of this article. The duration of the animation is 1 minute and it contains a total of 360 one-day-average optical SEDs, having six SEDs per frame. The observation dates of the SEDs are given in the plot legend. (An animation of this figure is available.)

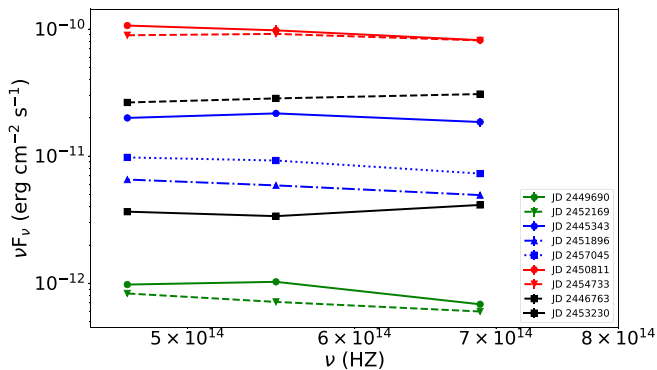


Figure 6. Examples of AO 0235+164 optical intraday SEDs during three different states of brightness: (i) the green lines represent SEDs during quiescent states (νF_ν (erg cm $^{-2}$ s $^{-1}$) $< 10^{-12}$), (ii) the blue lines show SEDs during moderately bright states ($10^{-12} < \nu F_\nu$ (erg cm $^{-2}$ s $^{-1}$) $< 3 \times 10^{-11}$), and (iii) the red lines show SEDs during outbursts (νF_ν (erg cm $^{-2}$ s $^{-1}$) $> 5 \times 10^{-11}$). The black lines are examples of SEDs with spectral hardening on JD 2,446,763 and JD 2,453,230.

the scaled C -statistic and F -statistic cross their respective critical values. We declare the final variability status of the blazar as variable/nonvariable if it is variable/nonvariable against all control stars. If the blazar is variable against only some of the control stars, we call it probably variable. We did not carry out the nested ANOVA test in a few data sets containing less than 20 observations. In the case of the power-enhanced F -test in the absence of the corresponding nested ANOVA test, we call the blazar probably variable even if the F -statistic crosses the critical value, as the F -test is more prone to giving a false-positive result (Zibecchi et al. 2017, 2020). If nested ANOVA is present and

both tests cross the critical values, we call the blazar variable. Otherwise, we declare the source nonvariable. We provide a summary of the IDV tests in Table 8. We give a final verdict on the variability status of the source after comparing the results of the combination of the C -test and F -test (C&F) from Table 6 and the results of the combination of the power-enhanced F -test and nested ANOVA test (P&N) from Table 7. If the results from both combinations are the same, we keep that result. If C&F declares “variable” and P&N declares “probably variable” due to the absence of nested ANOVA, we finally consider the source variable. We consider variability on 2005 November 8 as “nonvariable” because both the C -test and nested ANOVA result in nonvariability. Despite its being variable in nested ANOVA, we consider the 2005 December 5 lightcurve “nonvariable” as the F -test and power-enhanced F -test detect no variability. A few examples of DLCs of AO 0235+164 having different variability characteristics (variable/probably variable/nonvariable) are shown in Figure 8.

3.2.5. Doubling Timescale

The flux-doubling/halving timescale gives an estimate of the variability timescale (τ_{var}) of a source. We calculated the flux-doubling/halving timescale (τ_d) between two consecutive observations and its corresponding significance (σ) as

$$\mathcal{F}(t_{i+1}) = \mathcal{F}(t_i) * 2^{(t_{i+1}-t_i)/\tau_d}$$

$$\sigma = |\mathcal{F}(t_{i+1}) - \mathcal{F}(t_i)|/\varepsilon_i, \quad (12)$$

where $\mathcal{F}(t_i)$ and ε_i are the flux observed at time t_i and the corresponding measurement uncertainty, respectively. We considered the fastest doubling timescale (τ_d^{min}) with a higher

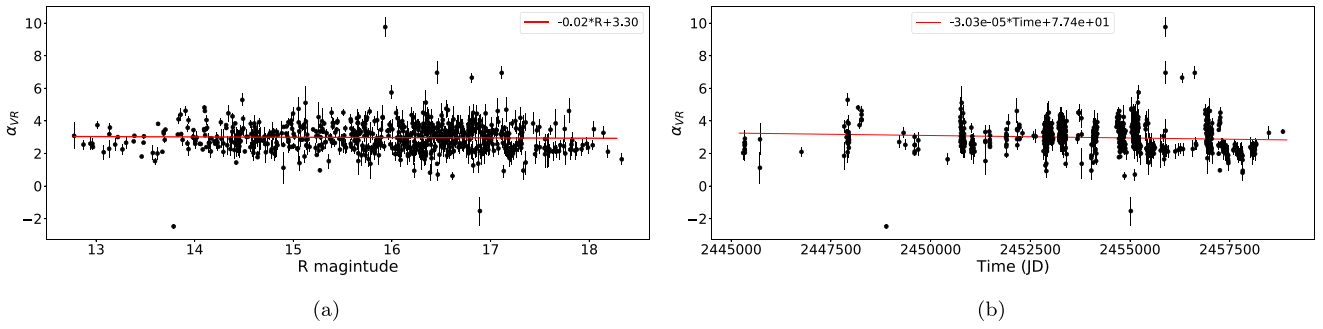


Figure 7. (a) Variation of the spectral index (α_{VR}) with R -band magnitude. (b) Variation of α_{VR} with time. The red line in each panel represents the linear fit.

Table 4

Spectral Index Variation with R -band Magnitude and Time in Optical $UBVRI$ Long-term Lightcurves of AO 0235+164

Dependency	m	c	ρ	p
α_{VR} vs. R	-2.01E-02	3.30E+00	-2.58E-02	4.92E-01
α_{VR} vs. JD	-3.03E-05	7.74E+01	-9.19E-02	1.39E-02

Note. Column headings: m = slope; c = intercept; ρ = Pearson coefficient; and p = null hypothesis probability for Figure 7.

significance than 3σ as an estimate for τ_{var} . We obtained $\tau_d^{\text{min}} < 1$ day for all nights when the source showed significant IDV in both the scaled F -test and the nested ANOVA test. This further strengthens our claims for the frequent presence of IDV. Following Equation (2) we computed the variability amplitudes on the same nights. All these results are listed in Table 7.

3.2.6. Duty Cycle

We calculated the duty cycle of AO 0235+164 using the definition of Romero et al. (1999), which was used later by multiple other authors (e.g., Stalin et al. 2009; Agarwal et al. 2016). The formula for the duty cycle for a particular wave band is given as

$$\text{DC} = 100 \frac{\sum_{i=1}^n N_i (1/\Delta t_i)}{\sum_{i=1}^n (1/\Delta t_i)} \% \quad (13)$$

where $\Delta t_i = \Delta t_{i,\text{obs}}/(1+z)$ (the duration of the monitoring session on the i th night is $\Delta t_{i,\text{obs}}$). Thus, this formula calculates the duty cycle weighted by the cosmological redshift corrected monitoring duration of each night. We set $N_i = 1, 0.5,$ and 0 for nights with a variability status of “variable,” “probably variable,” and “nonvariable,” respectively. We obtained a duty cycle for AO 0235+164 of $\sim 44\%$ in the V band and of $\sim 45\%$ in the R band considering the nights when the source was observed for at least 2 hr (Table 9).

3.3. The Mass of the Central Black Hole

We estimated the mass of the SMBH in AO 0235+164 by using its spectrum observed using the CCD Imaging/Spectropolarimeter at the Steward Observatory¹⁶ on 2011 January 8 (air mass = 1.12). This spectrum was selected since the blazar was then at its lowest level during the period 2008–2018, and it

¹⁶ <http://james.as.arizona.edu/~psmith/Fermi>

Table 5

Equivalence between Internal Field Star Numbering in the CASLEO/CAHA Data Used in the IDV Analyses and Field Star Numbering in Other Standard Star Charts during Different Observation Seasons

Season	CASLEO/CAHA	Heidelberg ^a	GKM2001 ^b
1999–2001 (CASLEO)	2 4 5 7 8 10 12	8 C1 6	10 9 11 1 3 8 16
2004–2005 (CASLEO)	2 4 5 6 7	8 C1 6	10 9 11 8 7
2005 (CAHA)	2 11 12 13 14 15 16 17	8 C1 6 ...	10 9 1 3 7 8 11 16
2018–2019 (CASLEO)	2 4 5 6 7 8	8 C1 6	10 9 11 8 7 16

Notes.

^a <https://www.lsw.uni-heidelberg.de/projects/extragalactic/charts/0235+164.html>

^b Gonzalez-Perez et al. (2001).

should ensure the best visibility of the emission lines because of the lower continuum contribution from the jet. The observed wavelength range of the spectrum we used is 4000–7550 Å, with a spectral resolution of 4 Å, and it was analyzed by following the procedure given in Liao & Gu (2020). First, it was corrected for Galactic extinction with the reddening map of Schlegel et al. (1998) and then was shifted to the rest-frame wavelength by using the redshift of 0.94.

This spectral coverage meant we could use the Mg II line, which is prominent on the spectrum shown in Figure 9 (focused on the 2400–3100 Å range), to estimate the SMBH mass. We

Table 6
Results of Scaled C -criterion and F -test for IDV on AO 0235+164 DLCs from CASLEO and CAHA

Date	JD	Band	No. of Obs.	S1, S2	Γ	C_T	F_T	$F_c^{0.005}$	Status	Final Status
1999 Nov 2	2,451,485	V	23	2, 3	0.8886	11.3640	129.1405	3.1246	V	V
				2, 6	1.0867	12.9184	166.8856	3.1912	V	
				2, 10	1.6876	8.1627	66.6298	3.1246	V	
				2, 11	0.7431	13.4002	179.5650	3.1246	V	
1999 Nov 3	2,451,486	V	22	2, 3	1.0707	5.6976	32.4624	3.1347	V	V
				2, 11	0.8841	6.0726	36.8768	3.1347	V	
1999 Nov 4	2,451,487	R	30	2, 3	1.0059	8.4058	70.6582	2.6737	V	V
				2, 11	0.6639	9.8857	97.7278	2.6737	V	
		V	30	2, 3	0.9994	8.9281	79.7104	2.6737	V	V
				2, 11	0.8286	9.6683	93.4770	2.6737	V	
1999 Nov 5	2,451,488	R	23	2, 3	1.4994	1.5631	2.4433	3.1246	NV	NV
				2, 11	0.9852	1.9303	3.7260	3.1246	NV	
		V	22	2, 3	1.4403	3.0342	9.2064	3.1347	V	V
1999 Nov 6	2,451,489	R	30	2, 3	0.8471	17.5775	308.9682	2.6737	V	V
				2, 6	0.9769	12.3281	151.9824	2.6737	V	
				2, 7	1.3573	9.9373	98.7501	2.7048	V	
				2, 8	1.3805	9.8381	96.7876	2.7048	V	
				2, 10	1.6936	6.8657	47.1376	2.6737	V	
				2, 11	0.5616	15.4338	238.2019	2.6737	V	
		V	29	2, 3	0.8485	18.1892	330.8486	2.7233	V	V
				2, 6	1.0013	11.7527	138.1254	2.7233	V	
				2, 7	1.3527	12.5480	157.4516	2.7397	V	
				2, 8	1.4133	13.4172	180.0214	2.7397	V	
		2, 10	1.5626	17.6674	312.1376	2.7233	V			
		2, 11	0.7018	17.9948	323.8145	2.7233	V			
1999 Nov 7	2,451,490	R	11	2, 3	0.9562	3.5930	12.9095	5.8479	V	PV
				2, 4	1.9798	2.2801	5.1990	5.8479	NV	
				2, 6	1.1143	4.3903	19.2751	5.8479	V	
				2, 10	1.9703	1.7073	2.9148	5.8479	NV	
				2, 11	0.6197	2.9496	8.7003	5.8479	V	
		V	12	2, 3	0.9382	2.9304	8.5871	5.3191	V	PV
				2, 4	1.7807	1.9342	3.7410	5.3191	NV	
				2, 6	1.1169	2.8931	8.3701	5.3191	V	
				2, 10	1.7653	2.1046	4.4292	5.3191	NV	
				2, 11	0.7772	4.3359	18.7997	5.3191	V	
2000 Dec 21	2,451,900	R	10	2, 3	0.9446	2.3638	5.5876	6.5402	NV	PV
				2, 6	1.0793	4.9877	24.8767	6.5402	V	
				2, 7	1.5020	2.0187	4.0753	6.5402	NV	
				2, 8	1.5289	1.9985	3.9939	6.5402	NV	
				2, 9	0.8790	2.5120	6.3100	6.5402	NV	
				2, 11	0.6246	7.4168	55.0085	6.5402	V	
		V	10	2, 3	0.9509	3.4671	12.0208	6.5402	V	PV
				2, 6	1.1202	2.4789	6.1449	6.5402	NV	
				2, 7	1.5357	1.8729	3.5079	6.5402	NV	
				2, 8	1.6064	2.0031	4.0124	6.5402	NV	
		2, 9	1.0966	3.7299	13.9120	6.5402	V			
		2, 11	0.7842	1.5920	2.5343	6.5402	NV			
2000 Dec 23	2,451,902	R	10	2, 3	0.8588	4.4475	19.7803	6.5402	V	V
				2, 6	0.9890	5.1629	26.6559	6.5402	V	
				2, 7	1.3855	3.5919	12.9020	6.5402	V	
				2, 8	1.4091	2.8222	7.9646	6.5402	V	
				2, 9	0.8000	4.6739	21.8451	6.5402	V	
				2, 11	0.5664	5.3690	28.8267	6.5402	V	
				2, 13	1.7083	3.0181	9.1089	6.5402	V	
		V	11	2, 3	0.8509	6.5241	42.5634	5.8479	V	PV

Table 6
(Continued)

Date	JD	Band	No. of Obs.	S1, S2	Γ	C_T	F_T	$F_c^{0.005}$	Status	Final Status
				2, 6	1.0031	5.4277	29.4602	5.8479	V	
				2, 7	1.3714	5.0139	25.1395	5.8479	V	
				2, 8	1.4341	5.2879	27.9619	5.8479	V	
				2, 9	0.9797	1.4805	2.1919	5.8479	NV	
				2, 11	0.7013	5.1765	26.7965	5.8479	V	
				2, 13	1.5668	4.3770	19.1586	5.8479	V	
2001 Nov 9	2,452,223	R	12	2, 11	1.2042	4.6476	21.5998	5.3191	V	V
		V	12	2, 3	1.8778	2.5035	6.2675	5.3191	NV	NV
				2, 4	3.6191	1.1450	1.3111	5.3191	NV	
				2, 9	2.2039	1.2380	1.5326	5.4171	NV	
				2, 10	3.5871	2.0056	4.0226	5.3191	NV	
				2, 11	1.5366	1.7566	3.0857	5.3191	NV	
2001 Nov 10	2,452,224	R	10	2, 3	2.3728	1.0570	1.1172	6.5402	NV	NV
				2, 9	2.2429	1.1058	1.2229	6.5402	NV	
				2, 11	1.5595	0.9395	0.8826	6.5402	NV	
		V	10	2, 3	2.3876	1.0788	1.1637	6.5402	NV	NV
				2, 9	2.7847	1.3860	1.9209	6.5402	NV	
				2, 11	1.9713	0.9038	0.8168	6.5402	NV	
2001 Nov 11	2,452,225	R	14	2, 3	2.0291	1.4125	1.9951	4.5724	NV	NV
				2, 9	1.5447	1.2505	1.5638	4.6425	NV	
				2, 11	1.3171	1.6860	2.8427	4.5724	NV	
		V	14	2, 3	2.0291	1.4125	1.9951	4.5724	NV	NV
				2, 9	1.5447	1.2505	1.5638	4.6425	NV	
				2, 11	1.3171	1.6860	2.8427	4.5724	NV	
2001 Nov 12	2,452,226	R	12	2, 3	1.8479	1.5819	2.5025	5.3191	NV	PV
				2, 11	1.2074	3.0203	9.1222	5.3191	V	
		V	12	2, 3	1.8704	1.9230	3.6980	5.3191	NV	NV
				2, 4	3.5981	1.0281	1.0571	5.3191	NV	
				2, 10	3.5672	2.3374	5.4634	5.3191	NV	
				2, 11	1.5330	1.5642	2.4468	5.3191	NV	
2001 Nov 13	2,452,227	R	11	3, 4	2.0213	1.1434	1.3073	5.8479	NV	NV
		V	11	3, 4	1.1840	0.6858	0.4703	5.8479	NV	NV
2005 Jan 16	2,453,387	R	11	2, 3	1.5238	3.8074	14.4962	5.8479	V	V
				2, 4	3.3465	2.7388	7.5010	5.8479	V	
				2, 6	3.3316	2.7442	7.5308	5.8479	V	
				2, 7	1.4051	3.4058	11.5996	5.8479	V	
2005 Nov 2	2,453,677	R	32	2, 3	1.2848	6.4237	41.2636	2.5846	V	V
				2, 4	0.8959	4.5227	20.4545	2.5846	V	
				2, 5	0.2571	4.3013	18.5013	2.5846	V	
				2, 6	0.5453	3.9310	15.4528	2.5846	V	
				2, 7	0.5844	4.9283	24.2884	2.5846	V	
				2, 8	0.4738	7.0560	49.7865	2.5846	V	
				2, 9	0.3415	6.5374	42.7373	2.5846	V	
				2, 10	0.3397	4.0828	16.6695	2.5846	V	
2005 Nov 4	2,453,679	R	12	2, 3	0.8534	4.3059	18.5409	5.3191	V	V
				2, 4	0.5599	3.7978	14.4235	5.3191	V	
				2, 5	0.1421	5.0805	25.8111	5.3191	V	
				2, 6	0.3029	5.3341	28.4524	5.3191	V	
				2, 7	0.3534	7.6846	59.0525	5.3191	V	
				2, 8	0.2839	4.3153	18.6220	5.3191	V	
				2, 9	0.1914	11.0664	122.4647	5.3191	V	
				2, 10	0.1875	5.4019	29.1804	5.3191	V	
2005 Nov 5	2,453,680	R	44	2, 3	0.9749	10.6766	113.9894	2.2266	V	V
				2, 4	0.6398	9.3431	87.2939	2.2266	V	

Table 6
(Continued)

Date	JD	Band	No. of Obs.	S1, S2	Γ	C_T	F_T	$F_c^{0.005}$	Status	Final Status
				2, 5	0.1942	11.0439	121.9674	2.2266	V	
				2, 6	0.3721	10.7338	115.2142	2.2266	V	
				2, 7	0.4059	10.2100	104.2433	2.2266	V	
				2, 8	0.3427	8.3494	69.7127	2.2266	V	
				2, 9	0.2399	12.1459	147.5239	2.2266	V	
				2, 10	0.2340	8.5775	73.5744	2.2341	V	
2005 Nov 6	2,453,681	R	40	2, 3	1.0022	7.8517	61.6495	2.3212	V	V
				2, 4	0.6946	8.8524	78.3645	2.3212	V	
				2, 5	0.2051	6.6830	44.6620	2.3212	V	
				2, 6	0.4022	7.6630	58.7211	2.3212	V	
				2, 8	0.3694	5.9489	35.3890	2.3212	V	
				2, 9	0.2576	6.8684	47.1751	2.3212	V	
				2, 10	0.2563	5.1520	26.5433	2.3212	V	
2005 Nov 8	2,453,683	R	28	2, 3	0.9329	2.4256	5.8834	2.7940	NV	NV
				2, 4	0.6336	2.3363	5.4585	2.7770	NV	
				2, 5	0.1788	1.7843	3.1836	2.7770	NV	
				2, 6	0.3598	2.2163	4.9120	2.7770	NV	
				2, 7	0.4059	1.4945	2.2335	2.7770	NV	
				2, 8	0.3451	2.1606	4.6682	2.9002	NV	
				2, 9	0.2318	1.3895	1.9307	2.7770	NV	
2005 Dec 5	2,453,710	R	20	2, 3	1.4796	1.4053	1.9748	3.4317	NV	NV
				2, 4	1.0247	0.7240	0.5242	3.4317	NV	
				2, 5	0.3133	0.9355	0.8752	3.4317	NV	
				2, 6	0.6030	1.1896	1.4151	3.4317	NV	
				2, 8	0.5634	1.0332	1.0674	3.4317	NV	
				2, 9	0.3979	1.0716	1.1482	3.4317	NV	
				2, 10	0.3915	0.8994	0.8089	3.4317	NV	
2005 Dec 6	2,453,711	R	16	2, 3	1.4092	2.1709	4.7129	4.0698	NV	PV
				2, 4	0.9785	3.7432	14.0118	4.0698	V	
				2, 5	0.2848	2.1323	4.5467	4.0698	NV	
				2, 6	0.5570	2.7562	7.5967	4.0698	V	
				2, 7	0.6157	1.8489	3.4186	4.0698	NV	
				2, 8	0.5266	1.3717	1.8815	4.0698	NV	
				2, 8	0.5266	1.3717	1.8815	4.0698	NV	
				2, 9	0.3691	2.4056	5.7869	4.0698	NV	
				2, 10	0.3688	2.0671	4.2727	4.0698	NV	
2019 Dec 17	2,458,835	R	30	9, 10	1.3151	1.2773	1.6315	2.6740	NV	NV
				9, 11	0.7377	1.3155	1.7307	2.6740	NV	
				9, 12	1.0425	1.0698	1.1445	2.6740	NV	

Note. S1 and S2 are the comparison and control star numbers, respectively, used for the IDV tests. The star numbers follow the star maps indicated in Table 5. In the final two columns, *V* means “variable,” *NV* means “nonvariable,” and *PV* means “probably variable.”

modeled the continuum by applying a single power law ($f_\lambda \propto \lambda^\alpha$) (as Fe II emission was rather weak). A Gaussian profile was then used to fit the Mg II line, centered at the position of 2800 Å, on the continuum-subtracted spectrum. The broad component of Mg II was fitted with a Gaussian with a 1000 km s⁻¹ lower limit, while a Gaussian with an upper limit of 1000 km s⁻¹ was applied for the narrow component. In order to estimate the corresponding errors of the FWHM and flux, we generated 100 mock spectra by adding random Gaussian noise to the original spectrum using the flux density errors and then took the standard deviations of measurements from those mock spectra as the uncertainties. Here, the flux density errors are the rms value of the spectrum calculated over the spectral window of (3000–3100) Å, after subtracting a second-order polynomial

function. Figure 9 shows the resulting fit to the spectrum. Our best-fitting results indicate that the line width of the broad Mg II component is $\text{FWHM} = 3151 \text{ km s}^{-1}$, with log-scale luminosity, in erg s⁻¹, $\log(L_{\text{Mg II}}) = 42.8$.

The line width and Mg II line luminosity we found are consistent with the range of values $\text{FWHM} = 3100\text{--}3500 \text{ km s}^{-1}$ and $\log(L_{\text{Mg II}}) = 42.5\text{--}42.8$, respectively, which were derived by Raiteri et al. (2007) from one Very Large Telescope and four TNG spectra of AO 0235+164 acquired in 2003–2004. We used the FWHM and luminosity of the broad Mg II line, not the continuum luminosity, as we were unable to exclude the jet emission contribution, despite the low-state spectrum that we could use for this blazar. The black hole mass was derived from the empirical relation used for Mg II

Table 7
Results of Power-enhanced F -test and Nested ANOVA Test for IDV on AO 0235+164 DLCs from CASLEO and CAHA

Obs. Date	Band	No. of Obs.	Power-enhanced F -test				Nested ANOVA Test			Status	Variability Amplitude (%)	Doubling Timescale (days)
			Comp. Stars	DOF (ν_1, ν_2)	F_{enh}	$F_c^{0.005}$	DOF (ν_1, ν_2)	F	$F_c^{0.005}$			
1999 Nov 2	V	23	2	(22, 87)	116.132	2.209	(5, 17)	58.924	5.075	V	43.99	0.103
1999 Nov 3	V	22	2	(21, 42)	34.529	2.540	(5, 16)	10.920	5.212	V	24.47	0.145
1999 Nov 4	V	30	2	(29, 58)	86.046	2.216	(7, 22)	38.922	4.109	V	34.48	0.106
	R	30		(29, 58)	82.016	2.216	(7, 22)	40.356	4.109	V	32.59	0.083
1999 Nov 5	V	22	2	(21, 21)	9.207	3.216	(5, 16)	4.426	5.212	NV	10.94	0.140
	R	23		(22, 44)	2.951	2.487	(5, 17)	9.426	5.075	V	9.03	0.335
1999 Nov 6	V	29	2	(28, 166)	211.363	1.960	(7, 21)	58.114	4.179	V	36.79	0.092
	R	30		(29, 170)	107.913	1.941	(7, 22)	74.686	4.109	V	37.90	0.085
1999 Nov 7	V	12	2	(11, 55)	6.392	2.854	PV	9.13	0.170
	R	11		(10, 50)	6.413	2.988	PV	5.36	0.244
2000 Dec 21	V	10	2	(9, 54)	4.813	3.055	PV	6.95	0.275
	R	10		(9, 54)	6.73	3.055	PV	7.67	0.428
2000 Dec 23	V	11	2	(10, 70)	10.314	2.846	PV	20.58	0.200
	R	10		(9, 63)	14.542	2.989	PV	14.18	0.180
2001 Nov 9	V	12	2	(11, 54)	2.345	2.863	NV	12.13	0.372
	R	12		(11, 22)	5.91	3.612	PV	12.73	0.441
2001 Nov 10	V	10	2	(9, 27)	1.152	3.557	NV	8.49	0.227
	R	10		(9, 27)	1.054	3.557	NV	5.64	0.660
2001 Nov 11	V	14	2	(13, 38)	2.02	2.923	NV	9.63	0.364
	R	14		(13, 38)	2.02	2.923	NV	9.63	0.364
2001 Nov 12	V	12	2	(11, 44)	2.212	2.969	NV	12.06	0.539
	R	12		(11, 22)	3.928	3.612	PV	11.74	0.856
2001 Nov 13	V	11	3	(10, 10)	0.470	5.847	NV	10.81	0.160
	R	11		(10, 10)	1.307	5.847	NV	10.19	0.178
2005 Jan 16	R	11	2	(10, 40)	9.842	3.117	PV	32.92	0.095
2005 Nov 2	R	32	2	(31, 247)	27.709	1.868	(7, 24)	37.156	3.991	V	8.98	0.189
2005 Nov 4	R	12	2	(11, 88)	31.995	2.689	V	6.59	0.166
2005 Nov 5	R	44	2	(43, 343)	124.459	1.713	(10, 33)	16.301	3.26	V	13.60	0.146
2005 Nov 6	R	40	2	(39, 273)	57.755	1.767	(9, 30)	87.95	3.45	V	9.79	0.227
2005 Nov 8	R	28	2	(27, 182)	4.371	1.965	(6, 21)	0.449	4.393	PV	3.18	0.365
2005 Dec 5	R	20	2	(19, 133)	1.067	2.200	(4, 15)	14.394	5.803	PV	2.61	0.391
2005 Dec 6	R	16	2	(15, 120)	4.863	2.373	PV	3.53	0.746
2019 Dec 17	R	30	9	(29, 87)	1.453	2.075	(7, 22)	2.341	4.109	NV	7.74	0.038

Note. Comparison star numbers follow the star maps indicated in Table 5. In the “Status” column, *V* means “variable,” *NV* means “nonvariable,” and *PV* means “probably variable.”

(Kong et al. 2006), which is based on measured broad-line region sizes in the reverberation-mapping AGN sample of Peterson et al. (2004), as

$$\frac{M_{\text{BH}}}{M_{\odot}} = 2.9 \times 10^6 \left(\frac{L_{\text{Mg II}}}{10^{42} \text{ erg s}^{-1}} \right)^{0.57 \pm 0.12} \left(\frac{\text{FWHM}_{\text{Mg II}}}{10^3 \text{ km s}^{-1}} \right)^2. \quad (14)$$

Thus, the SMBH mass is $\log(M_{\text{BH}}/M_{\odot}) = 7.90 \pm 0.25$, where the uncertainty is estimated from the measurement uncertainties of the FWHM and luminosity of Mg II. Using optical spectroscopy data from the Sloan Digital Sky Survey archive, Paliya et al. (2021) reported a somewhat higher mass, $\log(M_{\text{BH}}/M_{\odot}) = 8.58 \pm 0.34$, and an accretion disk luminosity (in erg s^{-1}) of $\log(L_{\text{disk}}) = 45.30 \pm 0.22$. Using the method mentioned in Paliya et al. (2021) with $\log(L_{\text{Mg II}}) = 42.8$, we obtained a lower disk luminosity (in erg s^{-1}) of $\log(L_{\text{disk}}) = 45.01 \pm 0.20$ from the spectrum observed on 2011 January 8.

4. Discussion

In this work, we have presented a detailed temporal and spectral study of the highly variable emission from the blazar AO 0235+164 observed at multiple optical wave bands (*UBVRI*) from 1975 October to 2019 December. The light-curves have highly uneven data sampling due to gaps in observation seasons and nonuniform observation campaigns. Although *U*-band data are quite sparsely sampled the *BVRI* observations have denser sampling when the source was highly active. Multiple long-term studies suggest that AO 0235+164 shows ~ 2 yr long flaring episodes with multiple subflares after intervals of ~ 8 yr (Raiteri et al. 2006; Fan et al. 2017; Roy et al. 2022). Figure 1 shows a difference of about 6 mag between the quiescent and outburst states in all optical wave bands, corresponding to an energy flux variation of more than 2 orders of magnitude (Figure 6). The long-term variability amplitudes at all five wave bands are quite similar (Table 1). Also, we found a strong correlation with zero time lag between the *UBVI* observations and the *R*-band data (Figures 2 and 3), which implies a common radiative process at a single emission

Table 8

Summary of Statistical Tests for IDV on AO 0235+164 DLCs from CASLEO and CAHA

Obs. Date	Band	Combined Variability Status		Final Status
		(<i>C</i> - and <i>F</i> -test) ^a	(PEF and N-ANOVA) ^b	
1999 Nov 2	V	V	V	V
1999 Nov 3	V	V	V	V
1999 Nov 4	V	V	V	V
	R	V	V	V
1999 Nov 5	V	V	NV	PV
	R	NV	V	PV
1999 Nov 6	V	V	V	V
	R	V	V	V
1999 Nov 7	V	PV	PV	PV
	R	PV	PV	PV
2000 Dec 21	V	PV	PV	PV
	R	PV	PV	PV
2000 Dec 23	V	PV	PV	PV
	R	V	PV	V
2001 Nov 9	V	NV	NV	NV
	R	V	PV	V
2001 Nov 10	V	NV	NV	NV
	R	NV	NV	NV
2001 Nov 11	V	NV	NV	NV
	R	NV	NV	NV
2001 Nov 12	V	NV	NV	NV
	R	PV	PV	PV
2001 Nov 13	V	NV	NV	NV
	R	NV	NV	NV
2005 Jan 16	R	V	PV	V
2005 Nov 2	R	V	V	V
2005 Nov 4	R	V	V	V
2005 Nov 5	R	V	V	V
2005 Nov 6	R	V	V	V
2005 Nov 8	R	NV	PV	NV
2005 Dec 5	R	NV	PV	NV
2005 Dec 6	R	PV	PV	PV
2019 Dec 17	R	NV	NV	NV

Notes. In the final three columns, *V* means “variable,” *NV* means “nonvariable,” and *PV* means “probably variable.”

^a Table 6.

^b Table 7; PEF = power-enhanced *F*-test.

zone is responsible for the bulk of the emission at the optical wave bands.

Sometimes during the quiescent states of powerful blazars, the disk thermal emission component becomes visible as a big blue bump on top of the synchrotron emission component from the jet in the optical–UV wave bands (e.g., Roy et al. 2021). As the disk emission is bluer than the jet synchrotron emission, an increase in jet activity during low-flux states displays a redder-when-brighter trend. The enhanced jet activity is observed when the charged particles inside the jet get accelerated to higher energies, and then radiate faster. Thus, the jet synchrotron component tends to get bluer with the increase in flux. If the jet emission completely outshines the disk emission, we expect to see a bluer-when-brighter trend (e.g., Isler et al. 2017). The flux increment can also be attributed to the increase of the jet Doppler factor (e.g., Papadakis et al. 2007), which blueshifts the spectrum and produces a bluer-when-brighter trend because of the convexity of the spectrum. Such a trend is seen in the (*B* – *I*) versus *R* magnitude diagram

(Figure 4(b)) and indicates the domination of nonthermal jet emission over the thermal emission component of the accretion disk during both flaring and quiescent states. From the convex shapes of the optical *BVR* SEDs during states ranging from quiescent to flaring (see the accompanying SED video and Figure 6), we may infer that the effect of the disk thermal emission is not significant in optical wave bands even during low-flux states.

This can be explained in terms of the nature of disk thermal emission given the disk luminosity and the central black hole mass computed in Section 3.3. The primary, and most precise, black hole mass estimation methods are based on stellar and gas kinematics and reverberation mapping (e.g., Vestergaard 2004). These methods need high spatial resolution spectroscopy data from the host galaxy and/or higher-ionization emission lines and are not applicable to most BL Lac objects. But in BL Lac objects, if weak emission lines are present, we can use the empirical methods (Kong et al. 2006) for black hole mass estimation. The most common parameters used for black hole mass estimation for BL Lac objects are the shortest variability timescales and periods of quasiperiodic oscillations (QPOs) (Gupta et al. 2012). Since BL Lac objects are highly variable objects, any black hole mass estimation may be treated as an upper limit, and there are possibilities of detection of a shorter variability timescale or a shorter QPO period. We obtained a log-scale black hole mass of 7.90 ± 0.25 in solar mass units. The Steward Observatory spectrum we used in our analysis has a narrower Mg II emission line (FWHM = 3151 km s^{-1}) than those of Raiteri et al. (2007) and Paliya et al. (2021), thus resulting in a lower mass estimate. We considered a multitemperature blackbody type accretion disk model, where the temperature at any portion of the disk is a function of the disk luminosity and the central black hole mass, to compute the thermal emission component. In Figure 10 we plot the thermal component along with the optical–UV SED during the lowest-activity state of AO 0235+164 observed on JD 2,452,169. It is evident that, as the thermal emission peaks at far-UV frequencies ($\sim 3.5 \times 10^{15} \text{ Hz}$) in the observer’s frame of reference, the jet emission always dominates in the *BVRI* wave bands. We do not see any significant trend in the variation of the (*V* – *R*) spectral index (α_{VR}) (Figure 7). The sudden rise of the *U*-band flux in Figure 10 is an indicator of a probable UV-soft X-ray bump as discussed in Raiteri et al. (2005, 2006). According to these studies, the source of the bump is either an additional synchrotron component coming from a separate emission region in the jet or the suppression of the emission of a continuous inhomogeneous jet in the near-UV region due to a discontinuity in opacity or misalignment of that particular emission region. Ackermann et al. (2012) mentioned that the whole optical–UV spectrum is produced by a single synchrotron-emitting zone as the shape of the bump does not change with luminosity. They attributed the UV spectral hardening to an artifact due to the overestimation of extinction by Junkkarinen et al. (2004).

For the detection of any statistically significant IDV in 33 lightcurves of AO 0235+164 observed at CASLEO/CAHA, we employed different statistical tests widely used in AGN variability studies. The reliability of each of these tests has been disputed (e.g., de Diego et al. 2015; Zibecchi et al. 2017), so we here employed a comparative approach that could allow us to circumvent the limitations affecting any individual test. In the first place, we used the scaled *C*-criterion and the *F*-test.

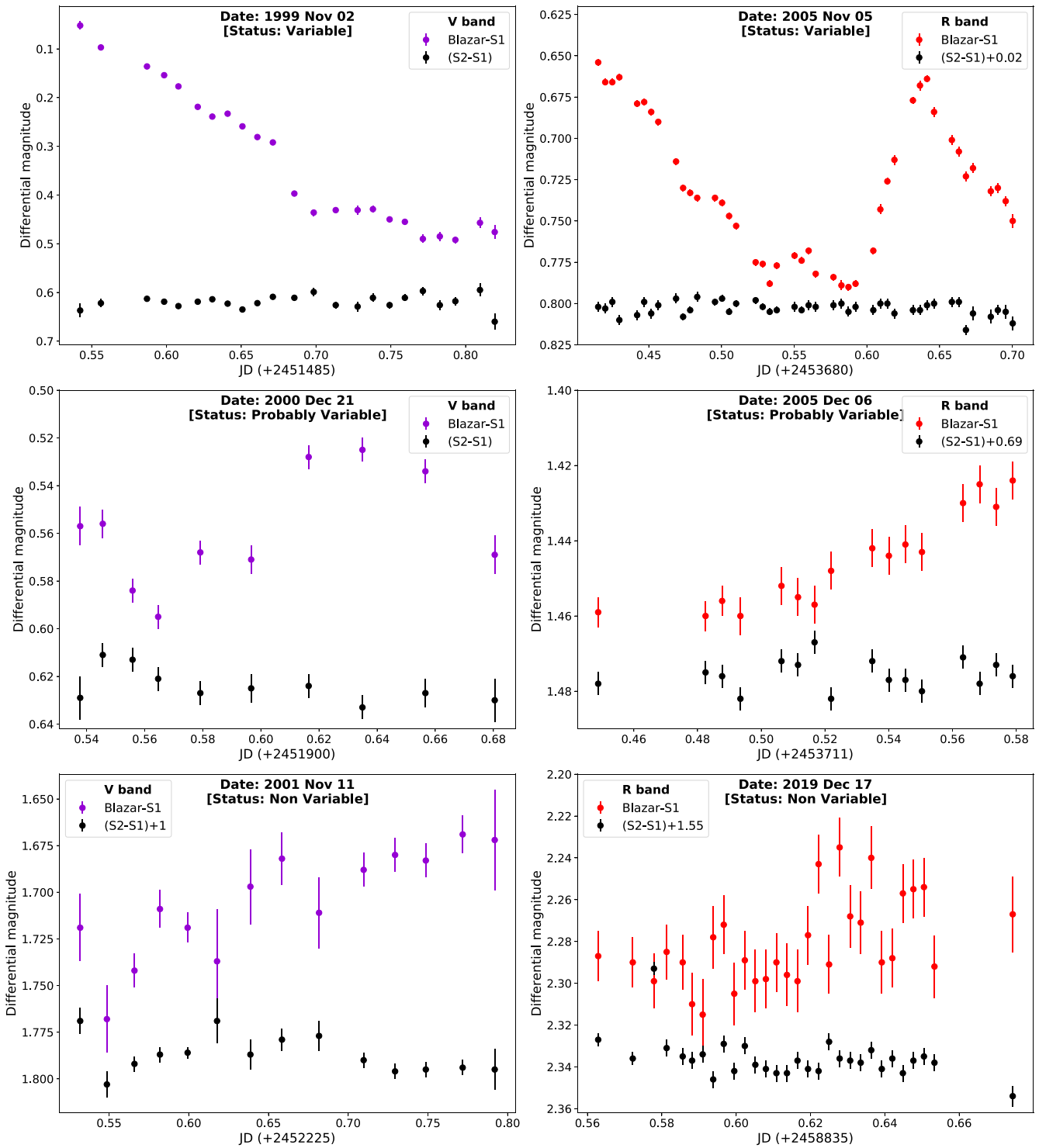


Figure 8. Some intraday lightcurves of AO 0235+164 on nights when the source showed different states of variability. S1 and S2 represent the comparison and control stars, respectively. In some panels, the DLC of the control star is shifted to bring it into the same frame of the blazar DLC for better visual comparison of variability.

The former compares the dispersion of the blazar lightcurve to the dispersion of a field star (control star), while the latter compares the variances. According to Zibecchi et al. (2017, 2020), the F -test has a tendency to classify noisy nonvariable curves as variable (i.e., to give false positives), while the C -criterion tends to give false negatives. Even though the C -criterion (Romero et al. 1999) cannot be considered an actual statistical test, it may still be a useful parameter for

detecting variability with high significance. The F -test, on the other hand, does not always work as expected, because it is particularly sensitive to non-Gaussian errors (“red noise”), which are usually an issue when analyzing blazar DLCs.

We also used the power-enhanced F -test and the nested ANOVA test, which involve multiple field stars. It is expected that the power-enhanced F -test may also suffer from the same drawback of detecting false variability as the original F -test. In

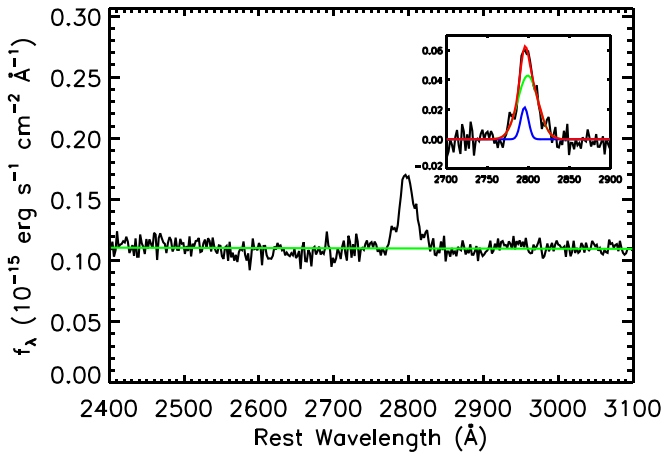


Figure 9. Spectral fitting of AO 0235+164, where the black curve is the original spectrum while the green line is the single power law for the fitted continuum. The inset shows the Mg II line fitting, where the blue, green, and red lines are the narrow, broad, and total components, respectively.

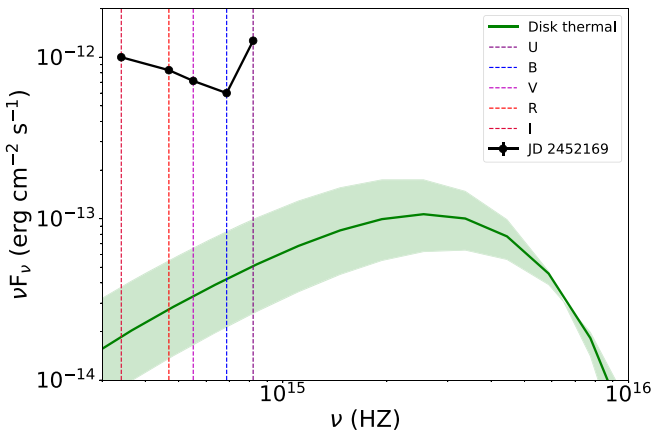


Figure 10. Comparison of the SED of the lowest-flux state observed on JD 2,452,169 and the thermal emission from the accretion disk in the observer’s frame. The thermal emission component is calculated using a multitemperature disk model with the black hole mass $\log(M_{\text{BH}}/M_{\odot}) = 7.9 \pm 0.25$, and the log-scale disk luminosity, in erg s^{-1} , $\log(L_{\text{disk}}) = 45.01 \pm 0.20$. The shaded region indicates the uncertainties in the calculation of the disk thermal component.

the nested ANOVA test, data grouping may also lead to false results if data within a time span larger than the (unknown) variability timescale are grouped. Comparing the results of Tables 6 and 7, while considering the tendencies of giving false results by the respective tests, we can confirm that the source is significantly variable in 4 out of 13 *V*-band lightcurves, and in 9 out of 20 *R*-band lightcurves. The source seems to be probably variable in three *V*-band and four *R*-band lightcurves, and nonvariable in the rest. On 1999 November 5, the combination of the *C*-criterion and *F*-test indicates nonvariability but the combination of the power-enhanced *F*-test and nested ANOVA detects variability in the *R*-band lightcurve. The results in the *V*-band lightcurve on that day are exactly the opposite. Similar situations were observed also on 2001 November 9 and 2001 November 12. A visual inspection of the DLCs of these nights reveals that the blazar DLCs are classified as nonvariable when either the control star DLC has higher variability (1999 November 5) or the measurement errors of the blazar DLCs are higher due to the blazar’s low-flux state (2001 November 9 and 12). Higher measurement

Table 9
Variation of Duty Cycle with the Duration of Observation in *R* Band

Observation Duration (hr)	No. of Nights	Duty Cycle (%)
>1	20	52
>2	19	45
>3	17	50
>4	14	57
>5	13	64
>6	8	77

errors lead to a lower chance of significant variability detection. These strange results may be an example of the drawbacks of the applied methods when trying to recover low-amplitude variations from DLCs affected by non-Gaussian noise (part of the observations on that night were taken at air mass >2 and under nonphotometric conditions). Otherwise, the combined results of the different methods seem to more or less agree. Alongside the optical SED patterns, such frequent IDV establishes AO 0235+164 as a low-energy-peaked BL Lac object (LBL). High-energy-peaked BL Lac objects (HBLs) show significantly less optical IDV than LBLs (Heidt & Wagner 1998; Romero et al. 1999).

The differences in IDV behavior have been attributed to the strength of magnetic fields present in the jet of HBLs. An axial magnetic field (B) higher than a critical value (B_c) may prevent the generation of any bends and Kelvin–Helmholtz instabilities in the jet base responsible for creating intraday microvariabilities. This indicates the presence of a weaker magnetic field than B_c in the jet of AO 0235+164. The critical magnetic field (B_c) is given in Romero (1995) as

$$B_c = \sqrt{4\pi n_e m_e c^2 (\Gamma^2 - 1)} / \Gamma, \quad (15)$$

where n_e is the electron density in the emission region, m_e is the electron rest mass, and Γ is the bulk Lorentz factor of the jet flow. Considering a typical set of parameters, $n_e = 429 \text{ cm}^{-3}$ and $\Gamma = 20$ (Ackermann et al. 2012), we get $B_c \simeq 0.07 \text{ G}$.

From Table 8 and Figure 8, we can say that the variability amplitudes were higher in the 1999 season when the source was in a fainter state (higher magnitude) than in the 2005 season. Marscher (2013) suggested that enhancement of flux can arise from a more uniform flow of particles inside the jet, which in turn decreases the amplitude of microvariability associated with turbulence inside the jet. Table 9 indicates that the probability of detection of significant variability increases with the duration of observation. Similar results for other blazars were found by Gupta & Joshi (2005), Rani et al. (2010), and Agarwal et al. (2016).

From the flux-doubling timescales listed in Table 7, we can estimate the upper limit to the size of the emission region (R_{max}) using the light travel time argument given as

$$R_{\text{max}} = \frac{c\delta t_{\text{var}}}{1+z} \quad (16)$$

where z is the cosmological redshift of 0.94, t_{var} is the variability timescale, and δ is the Doppler boost of the jet. Considering $\delta = 24$ (Hovatta et al. 2009) and t_{var} to be the shortest flux-doubling timescale of 0.083 days (when the source was significantly variable), we obtain an emission region size upper limit of $\sim 2.6 \times 10^{15} \text{ cm}$. Assuming a conical

jet model where the emission region fills up the entire jet cross section, we can estimate the probable maximum distance (d_{\max}) of the emission region from the central black hole as $d_{\max} = \Gamma R_{\max} = 5.2 \times 10^{16}$ cm. To explain the observed strong variability, Marchesini et al. (2016) attempted to apply a swinging jet model that attributes the observed variability to a change in the viewing angle of the emission region with time (i.e., a variation in the associated bulk Doppler factor). They reported a high rate of change in the viewing angle of about $7' - 10'$ per day, considering a mean viewing angle of 2.3° , would be necessary. However, they found that this geometric wiggling jet scenario was disfavored when considering the observed variation in color index with time. Several earlier studies on AO 0235+164 associated the observed fast optical variability with gravitational microlensing by the foreground absorber at $z = 0.524$. Webb et al. (2000) proposed that the 1997 flare resulted from microlensing because of an observed correlation with zero lag between the radio and optical lightcurves following Stickel et al. (1988), but the absence of any correlated flare in the X-ray lightcurve makes this explanation less likely. Abraham et al. (1993) and Raiteri et al. (2007) explained that such microlensing events can produce small amounts of fast flux amplification but are unlikely to dominate the high variability observed in AO 0235+164.

5. Conclusions

In this work, we conducted a study of long-term and short-term (intraday) variability in optical multiwaveband observations of the blazar AO 0235+164. Here we summarize our results and the probable physical scenarios.

1. We observed a variation of about 6 mag between the quiescent and flaring episodes, or over 2 orders of magnitude variation in the SEDs.
2. The *UBVI* lightcurves are highly correlated with the *R*-band lightcurve with zero time lag.
3. A significant bluer-when-brighter trend was observed in the (*B* – *I*) color variation with the *R* magnitude.
4. All the optical *BVR*-band SEDs show convexity. These observations indicate that the optical emission is dominated by jet radiation.
5. AO 0235+164 frequently shows statistically significant IDV in optical wave bands. This implies that AO 0235+164 is an LBL and probably has a weak magnetic field in the jet environment.
6. From the analysis of a broad Mg II emission line in a spectrum of AO 0235+164 taken at a low state, we estimate a central black hole mass of $\sim 7.9 \times 10^7 M_{\odot}$.

Data from the Steward Observatory spectropolarimetric monitoring project were used. This program is supported by Fermi Guest Investigator grants NNX08AW56G, NNX09AU10G, NNX12AO93G, and NNX15AU81G. This paper has made use of up-to-date SMARTS optical/NIR lightcurves that are available at www.astro.yale.edu/smarts/glast/home.php. This work is partly based on data taken and assembled by the WEBT collaboration and stored in the WEBT archive at Osservatorio Astrofisico di Torino–INAF (<https://www.oato.inaf.it/blazars/webt/>). These data are available upon request to the WEBT President Massimo













Villata (massimo.villata@inaf.it). This work is based on data acquired at Complejo Astronómico El Leoncito, operated under an agreement between Consejo Nacional de Investigaciones Científicas y Técnicas de la República Argentina and the National Universities of La Plata, Córdoba, and San Juan. We thank Anabella Araudo and Ileana Andruchow for their help with the observations made with CASLEO and the data analysis.

We thank the anonymous reviewer for very useful comments that helped us to improve the manuscript. We acknowledge the support of the Department of Atomic Energy, Government of India, under project identification No. RTI 4002. A.C.G. is partially supported by the Chinese Academy of Sciences President’s International Fellowship Initiative (PIFI) (grant No. 2016VMB073). G.E.R. acknowledges support from grants PIP 0554 and PIP 2021-1639 (CONICET) and grant PID2019-105510GBC31 of the Spanish Ministerio de Ciencia, Innovación y Universidades and through the Center of Excellence Mara de Maeztu 2020–2023 award to the ICCUB (CEX2019-000918-M). J.A.C. is a María Zambrano researcher fellow funded by the European Union’s NextGenerationEU (UJAR02MZ) and supported by PIP 0113 (CONICET) and PICT-2017-2865 (ANPCyT). J.A.C. was also supported by grant PID2019-105510GB-C32/AEI/10.13039/501100011033 from Agencia Estatal de Investigación of the Spanish Ministerio de Ciencia, Innovación y Universidades, and by Consejería de Economía, Innovación, Ciencia y Empleo of Junta de Andalucía as a member of research group FQM-322, as well as by FEDER funds.

Facilities: WEBT, CTIO:1.3m, Bok, SO:Kuiper, MMT, CASLEO:JST, CAO:2.2m.

Software: Astropy (Astropy Collaboration et al. 2013), DAOPHOT (Stetson 1987), IRAF (Tody 1986).

ORCID iDs

Abhradeep Roy  <https://orcid.org/0000-0002-4998-4560>
 Alok C. Gupta  <https://orcid.org/0000-0002-9331-4388>
 Varsha R. Chitnis  <https://orcid.org/0000-0001-5046-7504>
 Sergio A. Cellone  <https://orcid.org/0000-0002-3866-2726>
 Claudia M. Raiteri  <https://orcid.org/0000-0003-1784-2784>
 Gustavo E. Romero  <https://orcid.org/0000-0002-5260-1807>
 Paul J. Wiita  <https://orcid.org/0000-0002-1029-3746>
 Anshu Chatterjee  <https://orcid.org/0000-0003-0881-9275>
 Jorge A. Combi  <https://orcid.org/0000-0002-2565-5025>
 Mai Liao  <https://orcid.org/0000-0002-9137-7019>
 Arkadipta Sarkar  <https://orcid.org/0000-0002-7559-4339>
 Massimo Villata  <https://orcid.org/0000-0003-1743-6946>

References

- Abraham, R. G., Crawford, C. S., Merrifield, M. R., Hutchings, J. B., & McHardy, I. M. 1993, *ApJ*, 415, 101
 Ackermann, M., Ajello, M., Ballet, J., et al. 2012, *ApJ*, 751, 159
 Agarwal, A., Gupta, A. C., Bachev, R., et al. 2016, *MNRAS*, 455, 680
 Agudo, I., Marscher, A. P., Jorstad, S. G., et al. 2011, *ApJL*, 735, L10
 Astropy Collaboration, Robitaille, T. P., Tollerud, E. J., et al. 2013, *A&A*, 558, A33
 Bessell, M. S. 2005, *ARA&A*, 43, 293
 Bonning, E., Megan Urry, C., Bailyn, C., et al. 2012, *ApJ*, 756, 13
 Cellone, S. A., Romero, G. E., Combi, J. A., & Marti, J. 2007, *MNRAS*, 381, L60
 Cohen, R. D., Smith, H. E., Junkkarinen, V. T., & Burbidge, E. M. 1987, *ApJ*, 318, 577
 de Diego, J. A. 2014, *AJ*, 148, 93
 de Diego, J. A., Polednikova, J., Bongiovanni, A., et al. 2015, *AJ*, 150, 44

- Edelson, R. A., & Krolik, J. H. 1988, *ApJ*, 333, 646
- Fan, J. H., & Lin, R. G. 1999, *ApJS*, 121, 131
- Fan, J. H., Tao, J., Qian, B. C., et al. 2006, *PASJ*, 58, 797
- Fan, J. H., Kurtanidze, O., Liu, Y., et al. 2017, *ApJ*, 837, 45
- Fossati, G., Maraschi, L., Celotti, A., Comastri, A., & Ghisellini, G. 1998, *MNRAS*, 299, 433
- Gonzalez-Perez, J. N., Kidger, M. R., & Martin-Luis, F. 2001, *AJ*, 122, 2055
- Guo, Y. C., Hu, S. M., Xu, C., et al. 2015, *NewA*, 36, 9
- Gupta, A. C., Banerjee, D. P. K., Ashok, N. M., & Joshi, U. C. 2004, *A&A*, 422, 505
- Gupta, A. C., Fan, J. H., Bai, J. M., & Wagner, S. J. 2008, *AJ*, 135, 1384
- Gupta, A. C., & Joshi, U. C. 2005, *A&A*, 440, 855
- Gupta, S. P., Pandey, U. S., Singh, K., et al. 2012, *NewA*, 17, 8
- Hagen-Thorn, V. A., Larionov, V. M., Jorstad, S. G., et al. 2008, *ApJ*, 672, 40
- Heidt, J., & Wagner, S. J. 1996, *A&A*, 305, 42
- Heidt, J., & Wagner, S. J. 1998, *A&A*, 329, 853
- Hovatta, T., Valtaoja, E., Tornikoski, M., & Lahteenmaki, A. 2009, *A&A*, 494, 527
- Howell, S. B., Mitchell, K. J., & Warnock, A. I. 1988, *AJ*, 95, 247
- Ikejiri, Y., Uemura, M., Sasada, M., et al. 2011, *PASJ*, 63, 639
- Impey, C. D., Brand, P. W. J. L., & Tapia, S. 1982, *MNRAS*, 198, 1
- Isler, J. C., Urry, C. M., Coppi, P., et al. 2017, *ApJ*, 844, 107
- Itoh, R., Nalewajko, K., Fukazawa, Y., et al. 2016, *ApJ*, 833, 77
- Jang, M., & Miller, H. R. 1997, *AJ*, 114, 565
- Junkkarinen, V. T., Cohen, R. D., Beaver, E. A., et al. 2004, *ApJ*, 614, 658
- Kong, M.-Z., Wu, X.-B., Wang, R., & Han, J.-L. 2006, *ChJAA*, 6, 396
- Kutkin, A. M., Pashchenko, I. N., Lisakov, M. M., et al. 2018, *MNRAS*, 475, 4994
- Landolt, A. U. 2009, *AJ*, 137, 4186
- Liao, M., & Gu, M. 2020, *MNRAS*, 491, 92
- Madejski, G., Takahashi, T., Tashiro, M., et al. 1996, *ApJ*, 459, 156
- Marchesini, E. J., Andruchow, I., Cellone, S. A., et al. 2016, *A&A*, 591, A21
- Marscher, A. P. 1983, *ApJ*, 264, 296
- Marscher, A. P. 2013, *ApJ*, 780, 87
- Miller, H. R., Carini, M. T., & Goodrich, B. D. 1989, *Natur*, 337, 627
- Mucke, A., Protheroe, R. J., Engel, R., Rachen, J. P., & Stanev, T. 2003, *Aph*, 18, 593
- Nilsson, K., Charles, P. A., Pursimo, T., et al. 1996, *A&A*, 314, 754
- Paliya, V. S., Dominguez, A., Ajello, M., Olmo-Garcia, A., & Hartmann, D. 2021, *ApJS*, 253, 46
- Pandey, A., Gupta, A. C., Wiita, P. J., & Tiwari, S. N. 2019, *ApJ*, 871, 192
- Pandey, A., Gupta, A. C., Kurtanidze, S. O., et al. 2020, *ApJ*, 890, 72
- Papadakis, I. E., Villata, M., & Raiteri, C. M. 2007, *A&A*, 470, 857
- Peterson, B. M., Ferrarese, L., Gilbert, K. M., et al. 2004, *ApJ*, 613, 682
- Qian, S. J., Kraus, A., Witzel, A., Krichbaum, T. P., & Zensus, J. A. 2000, *A&A*, 357, 84
- Rabbette, M., McBreen, S., Steel, B., & Smith, N. 1996, *A&A*, 310, 1
- Raiteri, C. M., Villata, M., Capetti, A., et al. 2007, *A&A*, 464, 871
- Raiteri, C. M., Villata, M., Aller, H. D., et al. 2001, *A&A*, 377, 396
- Raiteri, C. M., Villata, M., Ibrahimov, M. A., et al. 2005, *A&A*, 438, 39
- Raiteri, C. M., Villata, M., Kadler, M., et al. 2006, *A&A*, 459, 731
- Raiteri, C. M., Villata, M., Larionov, V. M., et al. 2008, *A&A*, 480, 339
- Raiteri, C. M., Villata, M., Acosta-Pulido, J. A., et al. 2017, *Natur*, 552, 374
- Rani, B., Gupta, A. C., Strigachev, A., et al. 2010, *MNRAS*, 404, 1992
- Romero, G. E. 1995, *Ap&SS*, 234, 49
- Romero, G. E., Boettcher, M., Markoff, S., & Tavecchio, F. 2017, *SSRv*, 207, 5
- Romero, G. E., Cellone, S. A., & Combi, J. A. 1999, *A&AS*, 135, 477
- Romero, G. E., Cellone, S. A., & Combi, J. A. 2000, *A&A*, 360, L47
- Romero, G. E., Cellone, S. A., Combi, J. A., & Andruchow, I. 2002, *A&A*, 390, 431
- Roy, A., Patel, S. R., Sarkar, A., Chatterjee, A., & Chitnis, V. R. 2021, *MNRAS*, 504, 1103
- Roy, A., Chitnis, V. R., Gupta, A. C., et al. 2022, *MNRAS*, 513, 5238
- Sagar, R., Stalin, C. S., Krishna, G., & Wiita, P. J. 2004, *MNRAS*, 348, 176
- Schlegel, D. J., Finkbeiner, D. P., & Davis, M. 1998, *ApJ*, 500, 525
- Schramm, K. J., Borgeest, U., Kuehl, D., et al. 1994, *A&AS*, 106, 349
- Smith, P. S., Balonek, T. J., Heckert, P. A., Elston, R., & Schmidt, G. D. 1985, *AJ*, 90, 1184
- Smith, P. S., Montiel, E., Rightley, S., et al. 2009, arXiv:0912.3621
- Stalin, C. S., Kawabata, K., Uemura, M., et al. 2009, *MNRAS*, 399, 1357
- Stetson, P. B. 1987, *PASP*, 99, 191
- Stickel, M., Fried, J. W., & Kuehr, H. 1988, *A&A*, 198, L13
- Stickel, M., Fried, J. W., & Kuehr, H. 1993, *A&AS*, 98, 393
- Takalo, L. O., Sillanpaa, A., Valtaoja, E., et al. 1998, *A&AS*, 129, 577
- Tody, D. 1986, *Proc. SPIE*, 627, 733
- Urry, C. M., & Padovani, P. 1995, *PASP*, 107, 803
- Vestergaard, M. 2004, in ASP Conf. Ser. 311, AGN Physics with the Sloan Digital Sky Survey, ed. G. T. Richards & P. B. Hall (San Francisco, CA: ASP), 69
- Villata, M., Raiteri, C. M., Kurtanidze, O. M., et al. 2002, *A&A*, 390, 407
- Villata, M., Raiteri, C. M., Larionov, V. M., et al. 2008, *A&A*, 481, L79
- Villata, M., Raiteri, C. M., Gurwell, M. A., et al. 2009, *A&A*, 504, L9
- Wagner, S. J., & Witzel, A. 1995, *ARA&A*, 33, 163
- Wang, Y.-F., & Jiang, Y.-G. 2020, *ApJ*, 902, 41
- Webb, J. R., Howard, E., Benitez, E., et al. 2000, *AJ*, 120, 41
- White, R. J., & Peterson, B. M. 1994, *PASP*, 106, 879
- Wierzholska, A., Ostrowski, M., Stawarz, L., Wagner, S., & Hauser, M. 2015, *A&A*, 573, A69
- Woo, J.-H., & Urry, C. M. 2002, *ApJ*, 579, 530
- Zhang, B.-K., Jin, M., Zhao, X.-Y., Zhang, L., & Dai, B.-Z. 2021, *RAA*, 21, 186
- Zibecchi, L., Andruchow, I., Cellone, S. A., & Carpintero, D. D. 2020, *MNRAS*, 498, 3013
- Zibecchi, L., Andruchow, I., Cellone, S. A., et al. 2017, *MNRAS*, 467, 340